Characterizing typhoon-disturbed biomass dynamics using multitemporal airborne laser scanning and imagery, and deep learning in cool-temperate forest of northern Japan

（北日本の冷温帯林における複数時期の航空レーザ計測・写真と深層学習を用いた台風攪乱後バイオマス動態の解明）

Hokkaido University Graduate School of Agriculture
Frontiers in Environmental Studies Doctor Course

Ang Li

Abstract

Temperate forests are major carbon sinks, but post-disturbance biomass recovery is still difficult to quantify consistently at high spatial and temporal resolution. In northern Japan, Typhoon Songda (2004) caused extensive windthrow in the Tomakomai Experimental Forest and created a long-term need to separate immediate damage effects from delayed regrowth dynamics. This dissertation addresses that need by integrating field inventory data and multi-temporal remote sensing within one harmonized cross-year framework, so that interannual comparisons are not confounded by inconsistent processing scales.

Three LiDAR datasets (2004, 2014, and 2022) were compiled and harmonized to 2 m canopy height models (CHMs) across the overlapping 2,516 ha analysis domain after denoising and point-density normalization. Plot data from 2002, 2004, 2013, 2014, 2020, and 2021 were used to estimate biomass and calibrate a CHM-AGB allometric relationship, with each CHM year matched to temporally corresponding field observations. This calibrated relationship was then applied to each year's harmonized CHM to generate year-specific AGB maps at 2 m grid-cell resolution. Disturbed versus undisturbed areas were identified from 2004 color-infrared aerial imagery using deep learning (balanced accuracy on the test set = 92.2%), while needleleaf versus broadleaf crown types were classified from 6 cm UAV RGB imagery (balanced accuracy on the test set = 93.5%). In 2022, broadleaf forest occupied 93.3% of the mapped area and needleleaf forest occupied 6.7%, enabling explicit type-specific growth comparisons under both disturbed and undisturbed conditions. Across 2004–2022, mean growth rates were 0.13 m yr^{-1} for CHM and 1.30 Mg ha^{-1} yr^{-1} for AGB. Disturbed stands showed faster AGB increase than undisturbed stands (1.64 vs.

1.29 Mg ha^{-1} yr^{-1}). Within disturbed stands, AGB growth accelerated from 0.97 Mg ha^{-1} yr^{-1} in 2004–2014 to 2.48 Mg ha^{-1} yr^{-1} in 2014–2022, indicating a delayed but substantial recovery phase rather than an immediate post-typhoon rebound. At the whole-forest scale, mean CHM increased from 12.46 m to 14.86 m and mean AGB increased from 130.3 Mg ha^{-1} to 153.7 Mg ha^{-1} between 2004 and 2022. Growth-rate distributions also differed between disturbance classes and between needleleaf and broadleaf stands, showing persistent spatial heterogeneity in recovery pathways.

These results provide landscape-scale evidence that carbon recovery in cool-temperate forests after severe wind disturbance is significant but time-lagged. Methodologically, the study provides a practical workflow linking field plots, harmonized LiDAR structure, and image-based disturbance mapping for restoration planning and carbon accounting. The framework is transferable to disturbance-affected forests where repeated LiDAR and inventory data are available. Remaining uncertainty is mainly associated with CHM-AGB model formulation, attribution of localized negative growth patches, and inter-year data heterogeneity. Future work should incorporate independent validation datasets, uncertainty diagnostics, and management-history information to improve process attribution and further strengthen long-term recovery assessment. The same framework can support periodic updates as new LiDAR acquisitions become available, enabling consistent monitoring of recovery trajectories beyond the current 18-year window.

Table of Contents

List of Tables

List of Figures

List of Abbreviations

AGB	Aboveground biomass
CHM	Canopy height model
DBH	Diameter at breast height
DTM	Digital terrain model
GEDI	Global Ecosystem Dynamics Investigation
LiDAR	Light detection and ranging
RMSE	Root mean square error
UAV	Unmanned aerial vehicle

1 Introduction

1.1 Background

Forest aboveground biomass (AGB) recovery is important for climate mitigation because it influences how quickly disturbed forests can regain carbon uptake capacity (Anderson-Teixeira et al., 2013; Wang et al., 2021). Forest ecosystems absorb a substantial share of anthropogenic carbon emissions, and temperate forests are important contributors to this sink while also supporting multiple ecosystem services (Pan et al., 2011). However, this sink function can be sensitive to extreme disturbances (Wang et al., 2021; Cannon et al., 2023). Typhoons and other strong wind events can remove live biomass rapidly, alter canopy structure, and shift subsequent growth pathways over years to decades (Wu et al., 2019; Hayashi et al., 2015). For this reason, an important issue is not only the immediate loss after disturbance, but also the long-term trajectory through which structural recovery and biomass accumulation proceed (Yazaki et al., 2016; Wu et al., 2019).

Typhoon Songda affected Hokkaido in September 2004. It provides a well-documented case of severe wind disturbance in cool-temperate forests (Takahashi et al., 2011; Takano et al., 2016; Hayashi et al., 2015). Reported wind speeds exceeded 30–40 $\mathrm{m\,s^{-1}}$ in affected areas, and the disturbance produced extensive treefall and stem breakage (Hayashi et al., 2015; Takahashi et al., 2011), and site-level surface disturbance was also reported in post-

disturbance observations (Sano et al., 2010; Yazaki et al., 2016). In Hokkaido, severe damage was reported across approximately 370 km^2 of forest area (Takano et al., 2016; Hayashi et al., 2015). These immediate impacts define the initial condition from which medium- and long-term recovery should be evaluated, rather than treating post-disturbance forests as simple continuations of pre-disturbance growth trends (Sano et al., 2010; Yazaki et al., 2016).

The Tomakomai Experimental Forest offers a suitable setting for long-term recovery analysis because it contains heterogeneous stand conditions within a common regional climate context (Hiura, 2005; Hojo et al., 2023). The landscape includes naturally regenerated broadleaf stands as well as planted needleleaf stands, and areas with different disturbance histories can be characterized within the same broader region (Hiura, 2005; Hojo et al., 2023). This combination enables comparisons among disturbance classes and forest types under broadly comparable regional climate conditions (Hiura, 2005). It also provides practical relevance: post-disturbance handling, including salvage-related management in parts of the landscape, may interact with natural regeneration pathways and contribute to spatially variable recovery outcomes (Sano et al., 2010; Yazaki et al., 2016; Takano et al., 2016). As a result, Tomakomai is not only a case of disturbance impact but also a useful system for examining recovery heterogeneity.

A major challenge is that post-typhoon recovery can extend over multiple years and, in some systems, decades, whereas many observations are short-term or spatially sparse (Bartels et al., 2016; Hirata et al., 2014). Plot- and site-based measurements are important for ecological interpretation and calibration, but their spatial footprints are limited relative to landscape-scale disturbance mosaics (Matasci et al., 2018; Hayashi et al., 2015). Short

observation windows may emphasize immediate damage signals while providing less information on later recovery phases, and sparse sampling may miss localized contrasts in regrowth conditions (Decuyper et al., 2022; Hayashi et al., 2015). These constraints are especially important when the research question concerns how canopy structure and biomass recover across large areas with mixed disturbance histories (Matasci et al., 2018). Therefore, robust inference requires monitoring approaches that are both temporally extended and spatially continuous, rather than relying on either high detail at few points or broad coverage at a single time (Matasci et al., 2018; Decuyper et al., 2022).

Multi-temporal LiDAR is well suited to these conditions. It provides three-dimensional canopy information at high spatial resolution across entire landscapes (Hudak et al., 2012). However, interannual comparison of LiDAR-derived structural metrics is not straightforward: differences in acquisition settings, point density, and processing choices can introduce non-ecological contrasts unless data are carefully harmonized (Hudak et al., 2012; Loh et al., 2022). For long-term recovery assessment, cross-year consistency is an important methodological consideration (Hudak et al., 2012; Loh et al., 2022). In this thesis, this issue is addressed by harmonizing LiDAR-derived canopy height model (CHM) products across survey years and linking CHM to plot-based AGB through temporally matched calibration (Hudak et al., 2012; Loh et al., 2022). This framework supports year-specific AGB mapping on a common analytical basis and is intended to reduce methodological inconsistency in interannual comparisons. In addition, classifying disturbed versus undisturbed areas and forest-type classes can help provide a stratified basis for interpreting spatial heterogeneity in recovery patterns (Andersen et al., 2014; Borlaf-Mena et al., 2023; Hayashi et al., 2015).

Taken together, the background suggests the need for long-term, high-resolution, and cross-year consistent monitoring of post-typhoon forest recovery in cool-temperate systems (Hudak et al., 2012; Loh et al., 2022; Hayashi et al., 2015; Yazaki et al., 2016). The central motivation is not simply to apply LiDAR, but to address a forest-recovery problem that is difficult to resolve adequately using short-term or non-harmonized evidence alone. Within this context, the next section reviews previous studies to clarify what has been established, where important limitations remain, and how this thesis is positioned to address those limitations through an integrated CHM–AGB and classification-based framework.

1.2 Previous Studies

Previous studies have provided important evidence on forest response to disturbance, including immediate canopy damage, short-term biomass decline, and early regrowth tendencies (Hayashi et al., 2015; Sano et al., 2010; Wu et al., 2019). Research on wind disturbance has clarified that structural impacts can be severe and spatially heterogeneous, and that recovery pathways vary with stand condition and disturbance intensity (Hayashi et al., 2015; Takano et al., 2016; Wu et al., 2019). In Japanese and Hokkaido contexts, studies related to Typhoon Songda have documented substantial damage and subsequent ecological change (Hayashi et al., 2015; Sano et al., 2010; Takano et al., 2016). These findings establish a strong foundation. At the same time, evidence is still uneven in terms of observation duration, spatial continuity, and cross-year comparability, which limits synthesis for long-term biomass recovery at landscape scales (Coops et al., 2021; De Marzo et al., 2023).

Field inventory and plot-based approaches continue to provide a core basis for biomass estimation and ecological interpretation (Hudak et al., 2012; Brede et al., 2022). They provide species-level and tree-level information that remote sensing alone cannot fully replace, and they are essential for calibration and validation of structural proxies. Flux-tower observations also contribute to understanding ecosystem carbon exchange dynamics (Sano et al., 2010; Wu et al., 2019). However, these approaches are often constrained by plot distribution, repeated-survey logistics, and representativeness across heterogeneous disturbance mosaics (Hayashi et al., 2015; Brede et al., 2022; Coops et al., 2021). When disturbance and recovery vary strongly across space, inference from sparse plot networks may not capture full landscape variability. Consequently, plot and tower approaches are highly valuable but typically insufficient by themselves for wall-to-wall reconstruction of long-term post-disturbance biomass trajectories (Hudak et al., 2012; Coops et al., 2021).

Remote sensing has expanded observation coverage and enabled broader assessments of forest change. Optical imagery is widely used for disturbance detection and land-cover characterization, while LiDAR provides direct structural information that is especially relevant for canopy-height-based biomass inference (Hayashi et al., 2015; Hudak et al., 2012). Despite these advances, many studies still rely on short temporal spans or structurally limited observation histories, which can limit the ability to resolve medium- to long-term recovery heterogeneity (Coops et al., 2021; De Marzo et al., 2023). In addition, studies often differ in processing workflows, making cross-study comparison difficult (Coops et al., 2021; Hudak et al., 2012). Thus, previous remote-sensing work has improved detection capacity but has not fully resolved the combined requirement of long duration, high resolution, and internally consistent interannual analysis for disturbance-recovery research (Coops et al., 2021; Hudak et al., 2012; De Marzo et al., 2023).

Within LiDAR-focused studies, a key issue is cross-year harmonization. Even when multiple survey years are available, differences in point density, flight conditions, and processing pipelines can influence derived CHM and downstream biomass estimates (Khosravipour et al., 2016; Hudak et al., 2012). Without explicit harmonization, observed temporal differences may partly reflect methodological inconsistency rather than ecological change (Khosravipour et al., 2016; Hudak et al., 2012). This concern is particularly relevant when early-year data are sparse and later-year data are dense, as is common in long-term archives (Hudak et al., 2012; Khosravipour et al., 2016). Previous literature has recognized the technical importance of scale and processing choices in CHM generation (Khosravipour et al., 2014, 2016), but fully harmonized workflows tied to long-term post-typhoon biomass recovery remain relatively limited, especially in cool-temperate post-typhoon contexts (Hudak et al., 2012; Hayashi et al., 2015; Yazaki et al., 2016).

Another gap is the limited integration of disturbance-history and forest-type stratification within one consistent recovery framework (Hayashi et al., 2015; De Marzo et al., 2023; Knapp et al., 2020). In practice, this limitation is reflected in the fact that disturbance-history and major forest-type contrasts are not always examined together within a single recovery framework (Requena Suarez et al., 2023; Knapp et al., 2020). This can obscure interpretation of whether recovery differences arise mainly from disturbance legacy, forest composition, or their interaction (De Marzo et al., 2023; Knapp et al., 2020). For management-relevant inference, it is important to compare trajectories across disturbed and undisturbed conditions and across needleleaf- and broadleaf-dominated areas under a unified analytical design (Hayashi et al., 2015; De Marzo et al., 2023; Knapp et al., 2020). Such stratified comparison helps reveal spatial heterogeneity that is difficult to infer from single aggregated means.

Overall, previous studies indicate three persistent needs for robust long-term recovery assessment: temporally extended observation, high-resolution landscape coverage, and cross-year harmonization within one analytical framework (Hudak et al., 2012; Yazaki et al., 2016; Bartels et al., 2016). These needs directly motivate the design of this thesis. By integrating harmonized multi-temporal LiDAR products, plot-calibrated CHM–AGB estimation, and image-based classification of disturbance and forest type, the study aims to provide a consistent basis for interannual comparison from 2004 to 2022 in the Tomakomai Experimental Forest. This positioning links established knowledge from prior work with a targeted methodological response to remaining limitations, and it leads directly to the objectives defined in the next section.

1.3 Objectives

The main objective of this dissertation is to quantify long-term post-typhoon recovery of canopy structure and aboveground biomass (AGB) in a cool-temperate forest using a harmonized multi-temporal remote-sensing framework.

The specific objectives are as follows.

1. To harmonize airborne LiDAR datasets from 2004, 2014, and 2022 into consistent 2 m canopy height model (CHM) products, and to calibrate a CHM–AGB relationship using temporally matched field observations for year-specific AGB mapping.

2. To identify typhoon-disturbed and undisturbed areas from 2004 color-infrared aerial imagery, and to classify needleleaf and broadleaf forest areas from high-resolution UAV imagery using deep-learning-based image analysis.

3. To quantify and compare changes in CHM and AGB, including annual growth rates, across 2004–2014, 2014–2022, and 2004–2022 among disturbance classes and forest types, in order to characterize spatial heterogeneity and temporal lag in post-disturbance recovery.

1.4 Thesis Structure

This dissertation is organized into five chapters. Chapter 1 presents the background, previous studies, research objectives, and overall scope of the study. Chapter 2 describes the methodological framework, including the study area, multi-temporal LiDAR and field data processing, deep-learning-based disturbance and tree-type classification, and analytical procedures used to quantify forest growth dynamics. Chapter 3 presents the main results, including classification accuracy, spatial disturbance patterns, and temporal changes in canopy height model (CHM) and aboveground biomass (AGB) from 2004 to 2022. Chapter 4 discusses these findings in relation to previous studies, interprets post-typhoon recovery processes, and addresses limitations and future research directions. Chapter 5 summarizes the main conclusions and highlights the methodological and practical implications for long-term biomass monitoring and restoration planning in disturbance-affected cool-temperate forests.

2 Methods

The main methodological steps of this study (Fig. 2.1) are as follows: (i) LiDAR scanning and data processing: high-resolution canopy height models (CHMs) are generated through data denoising, sampling, and resampling, and aboveground biomass is estimated; (ii) identification of typhoon disturbance areas: disturbed areas affected by typhoons are automatically identified and distinguished from undisturbed areas using aerial imagery and deep learning models; (iii) identification of needleleaf and broadleaf forest areas: the distribution of needleleaf and broadleaf tree regions within the forest is classified directly from UAV imagery using deep learning algorithms; and (iv) analysis of forest growth and recovery patterns.

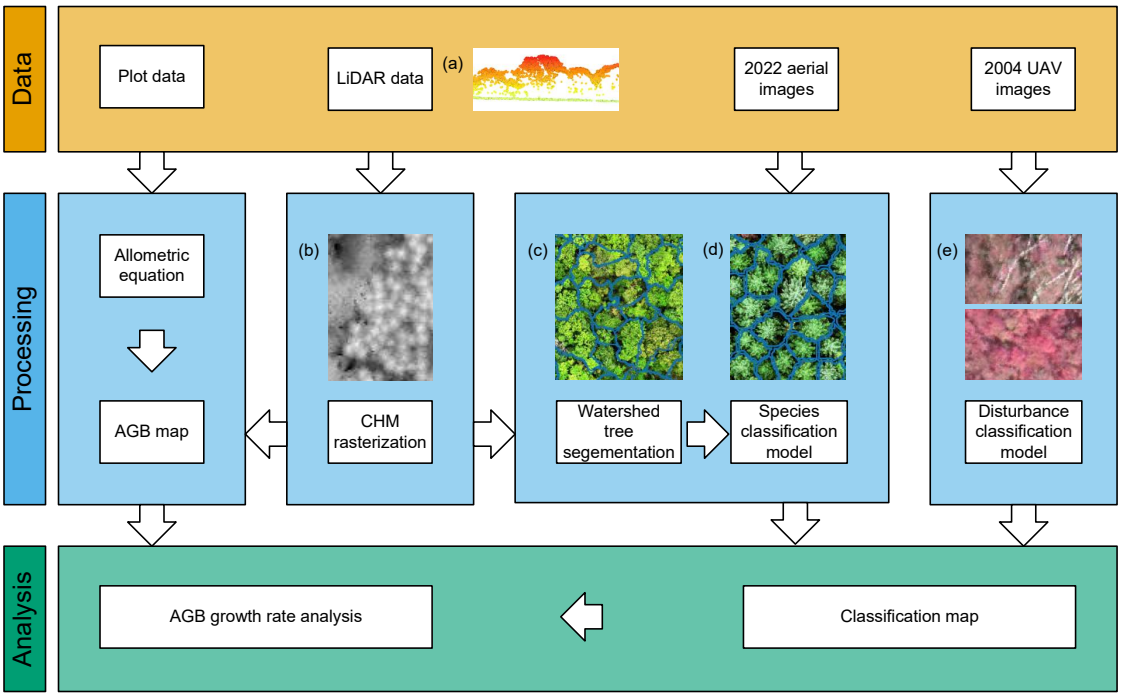

Fig. 2.1. Flowchart of the study. (a) 2014 LiDAR point cloud, (b) 2022 CHM, (c) 2022 UAV imagery with individual tree segmentation results in the broadleaf-dominated area, (d) 2022 UAV imagery with individual-tree segmentation results in the needleleaf-dominated area, and (e) comparison of two 2004 aerial images of forests with and without windthrow disturbance.

2.1 Study areas

The study was conducted in the Tomakomai Experimental Forest at Hokkaido University, Japan (Fig. 2.2). As shown in Fig. 2.2(b), a regional locator map places the study area in the Japan–Asia context, and the Hokkaido region containing the study area is highlighted

with a yellow rectangle. The forest spans a latitude range from 42°38′ N to 42°46′ N and a longitude range from 141°33′ E to 141°42′ E. The average annual temperature in this region is 6.7 °C, with extremes ranging from −22 °C to 28 °C. The area receives an annual precipitation of approximately 1,112 mm and has an elevation range of 20–90 m above sea level. The forest is characterized by naturally grown deciduous broad-leaved trees such as *Quercus crispula*, *Magnolia obovata*, *Tilia japonica*, *Padus ssiori*, and *Acer mono*, among others. Additionally, there are artificial plantation forests of needleleaf species, including *Larix kaempferi*, *Abies sachalinensis*, and *Picea glehnii*. In addition to the regional map (Fig. 2.2), representative field photographs are provided to illustrate local canopy and interior stand conditions within the study area (Fig. 2.3).

Although typhoon approaches are less frequent in Hokkaido than in southern Japan, post-disturbance handling in Tomakomai included salvage operations. Subsequent regeneration processes can influence recovery trajectories (Sano et al., 2010; Takano et al., 2016).

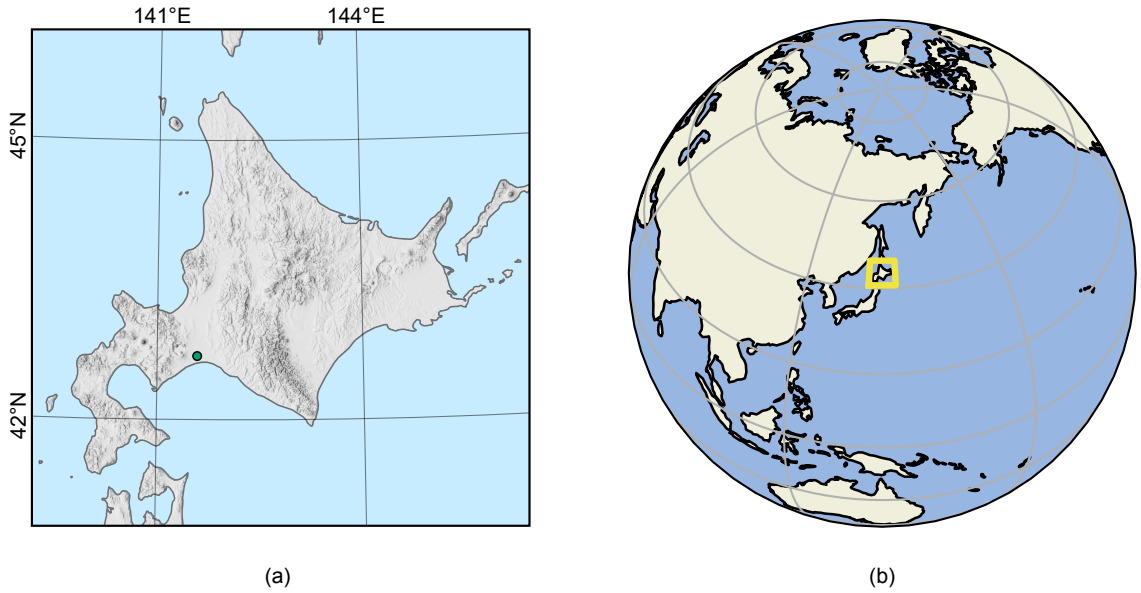

Fig. 2.2. Location of the Tomakomai Experimental Forest in Hokkaido, Japan. (a) Detailed map of Hokkaido showing the centroid of the study area. (b) Regional locator map of East Asia and Japan; the yellow rectangle highlights the Hokkaido region containing the study area.

Fig. 2.3. Representative field photographs from the Tomakomai Experimental Forest. Top: representative local canopy view within the study area. Bottom: representative interior stand condition showing understory vegetation and downed woody debris.

2.2 LiDAR data

We used data from three LiDAR surveys. The first LiDAR dataset was acquired on 23 September 2004, 15 days after the typhoon, using an airborne LiDAR system operated by the National Institute for Environmental Studies. The average point density was 1.6 points m^{-2}. The second LiDAR survey was conducted in October 2014 by the Ministry of Land, Infrastructure, Transport, and Tourism (MLIT), using a LiDAR sensor mounted on an AS350 helicopter. The average point density was 33.2 points m^{-2}. The third LiDAR dataset was obtained in August 2022 via a drone-mounted LiDAR sensor operated by the Field Science Center for the Northern Biosphere, Hokkaido University. The average point density was 157.3 points m^{-2}.

CHMs were generated at 2 m spatial resolution from airborne LiDAR data. The overlapping areas of 2,516 ha in multiple LiDAR flights were analyzed, and non-forest areas including high-voltage electricity transmission lines, buildings, and roads were eliminated. First, noise reduction was applied to all three datasets. The point clouds from the three datasets were subsequently resampled to retain one random point per square meter, to approximate the lower-density condition of the 2004 survey and maintain consistent point cloud density across the three years. Reducing point density is known to lower CHM-derived canopy heights (Garcia et al., 2017; Roussel et al., 2017), necessitating density normalization before cross-year comparison. Afterwards, the point cloud was divided into ground and non-ground points, and the height of the non-ground points relative to the ground surface was computed. Finally, we rasterized the normalized heights of non-ground points to produce pit-free, LiDAR-derived CHM rasters at 2 m resolution (Khosravipour et al., 2014). For

clarity, harmonized 2 m CHMs were generated for 2004, 2014, and 2022 and used as year-specific canopy-height inputs for interannual AGB estimation. The interannual AGB estimation workflow is based on harmonized multitemporal CHMs and plot-level calibration, and UAV data in this study served as one data source rather than a methodological prerequisite. Following prior work, raster cell size was selected to be commensurate with typical LiDAR sampling support rather than substantially finer than it (Khosravipour et al., 2016). To evaluate this in the sparsest survey year, we analyzed the edge-length distribution of the 2004 LiDAR TIN constructed from last-return points (Fig. 2.4). The median edge length was 0.968 m and the 95th percentile was 2.002 m, supporting the use of a harmonized 2 m grid for interannual CHM mapping.

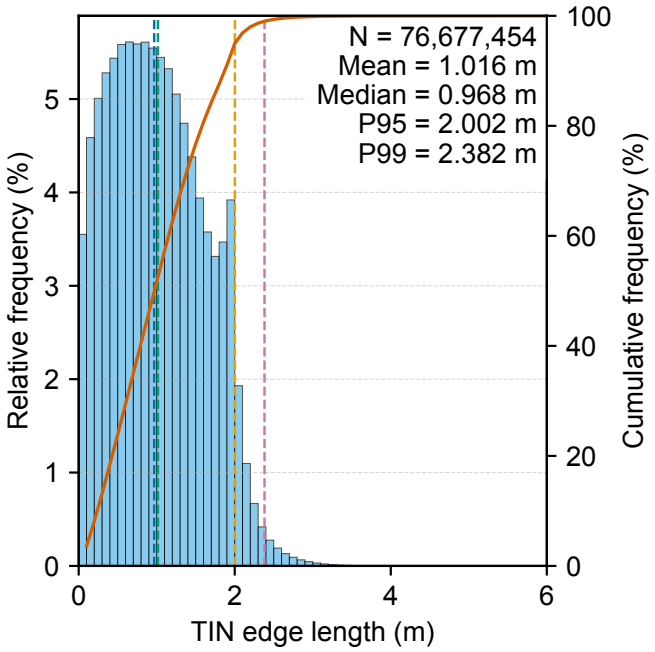

Fig. 2.4. TIN edge-length distribution from 2004 LiDAR last-return points used for resolution-support diagnostics. Histogram bins are 0.1 m. Bars show relative frequency (left axis), and the orange curve shows cumulative frequency (right axis). Vertical dashed lines indicate the mean (green, 1.016 m), median (blue, 0.968 m), the 95th percentile (orange, 2.002 m), and the 99th percentile (reddish purple, 2.382 m).

2.3 Field data

The field data are used to calculate average AGB within each plot and to regress these values against the corresponding plot-level average CHM, thereby deriving an allometric equation relating CHM to AGB that is applicable across the entire study area. Although

plot surveys are essential for calibration and validation, their limited spatial coverage and temporally discontinuous observations cannot provide wall-to-wall interannual AGB mapping across the 2,516 ha landscape. We used forest-plot survey data from the Tomakomai Experimental Forest for 2002, 2004, 2013, 2014, 2020, and 2021, including information on tree species and diameter at breast height (DBH). We used 114 unique RTK-surveyed field plots, corresponding to 165 plot-year observations across six survey years: 2002 (n=27), 2004 (n=20), 2013 (n=25), 2014 (n=40), 2020 (n=33), and 2021 (n=20). Tree height (H, m) was estimated from diameter at breast height (D, cm) following the method originally proposed by Ogawa (1969):

$$\frac{1}{H} = \frac{1}{aD^h} + \frac{1}{H_{\max}} \tag{2.1}$$

The equation was calibrated with measurements from 3,966 trees in the study area, yielding a root mean square error (RMSE) of 2.09 m. Here, $H_{\max} = 28.86$ m is the maximum observed tree height, and the fitted coefficients are $a = 1.28$ and $h = 1.04$. Equation (2.1) was used only to estimate tree height from DBH and was not directly used to compute AGB. The DBH, estimated tree height, and wood density were used to calculate tree dry mass following Ishihara et al. (2015). Wood density was assigned by species lookup whenever available. For tree records matched to the 165 plot-year calibration dataset, wood density was missing for 3.14% of records (951/30,263), and AGB for those records was estimated using DBH and estimated tree height only. The plot data also included plot boundaries measured using real-time kinematic (RTK) positioning, from which the plot area was calculated. Summing the biomass of all trees in a plot and dividing by the plot area yielded

the mean biomass density of the plot, expressed in Mg ha^{-1}.

The mean CHM value for each plot was subsequently calculated. For calibration, plot-mean CHM was extracted from each year's harmonized 2 m CHM within RTK-surveyed plot boundaries, using each 2 m CHM pixel's overlap area with the RTK-surveyed plot polygon (m^2) as weights, ensuring that both predictor (CHM) and response (plot AGB) were defined on the same plot-level spatial support. These values were matched to temporally corresponding plot-level AGB estimates (Mg ha^{-1}): the 2004 CHM with 2002 and 2004 AGB estimates, the 2014 CHM with 2013 and 2014 AGB estimates, and the 2022 CHM with 2020 and 2021 AGB estimates. Scatterplots were then generated to establish a linear CHM–AGB allometric relationship. This relationship was subsequently applied to each year's harmonized 2 m CHM to produce year-specific AGB maps for 2004, 2014, and 2022, enabling consistent comparisons between disturbed and undisturbed stands.

2.4 Identification of typhoon-disturbed areas

This study utilized 118 multispectral images, including near-infrared, red, and green bands, which were collected in 2004 over the Tomakomai Experimental Forest using airborne sensors. The images were orthorectified and mosaicked into a single seamless orthophoto with a spatial resolution of 0.2 m.

To prepare the data for model training and validation, the orthophoto was divided into 25 m^2 tiles using a 5 m grid. A random sample of tiles totaling 161.26 ha was then man-

ually interpreted and each selected tile was labeled as either “disturbed” or “undisturbed” on the basis of visual inspection. A tile was classified as “disturbed” when wind-thrown tree damage could be clearly identified in the imagery, whereas tiles that showed no visible windthrow signature were classified as “undisturbed.” The dataset was then split into training and validation sets, with 90% of the data used for training and 10% for validation. For final performance evaluation, we used an independent spatially separated test set that was not split from the original training/validation data. Fig. 2.5(c) and Fig. 2.5(d) show representative examples of aerial imagery used for training and validating the deep learning model, illustrating the contrast between undisturbed (c) and typhoon-disturbed (d) forest conditions. The landscape-scale context and locations of these representative patches are shown in Fig. 2.6(a).

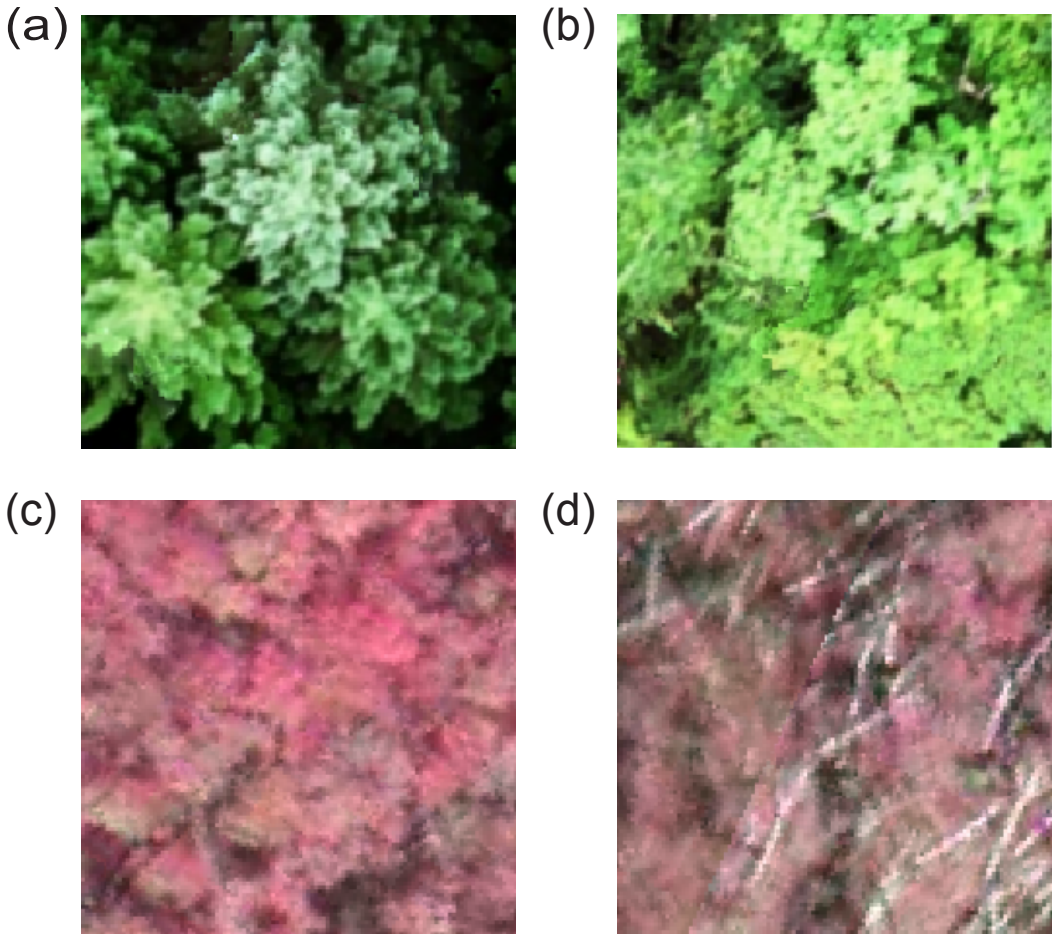

Fig. 2.5. Representative images used for deep learning-based classification and disturbance detection. This figure illustrates the types of data that can be used for training and validating deep learning models, including (a) a 2022 UAV image of a needleleaf forest, (b) a 2022 UAV image of a broadleaf forest, (c) a 2004 aerial image of an undisturbed forest, and (d) a 2004 aerial image of a typhoon-disturbed forest.

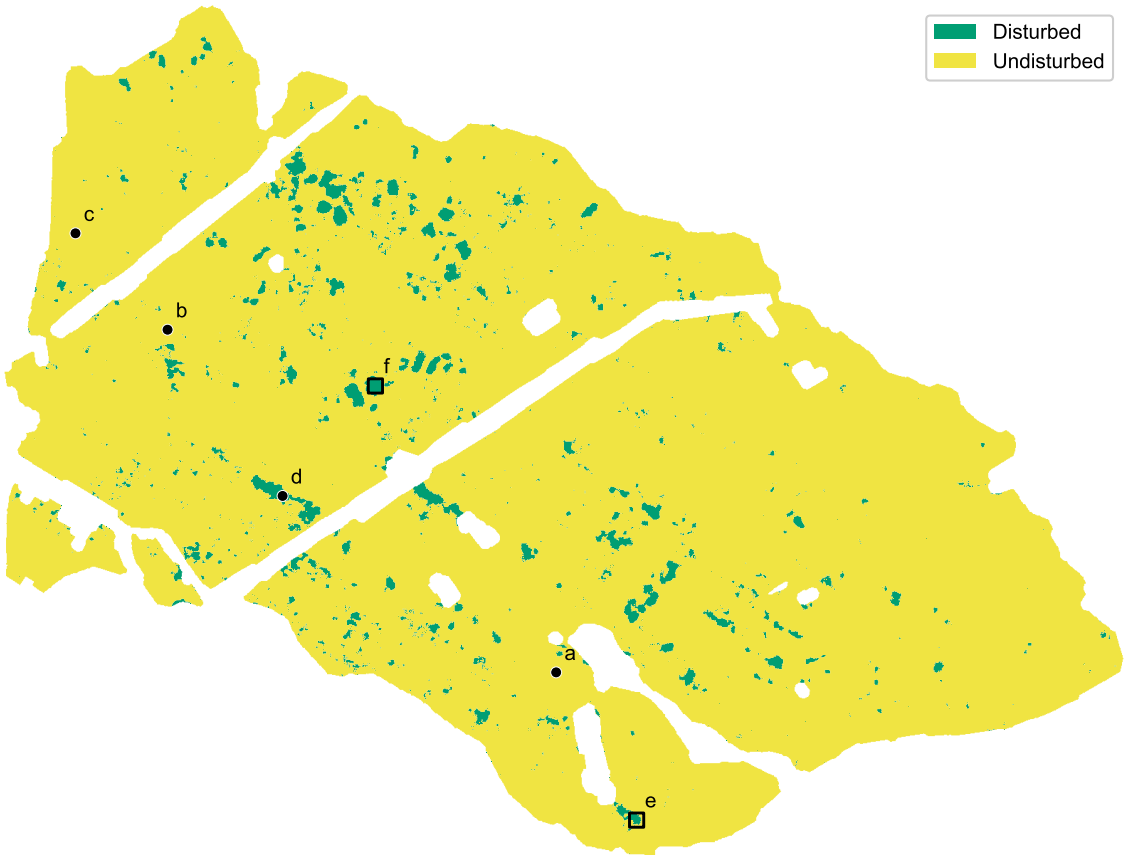

(a)

Fig. 2.6. Landscape-scale disturbance context and locations of representative image patches. Panel (a) shows the study-wide distribution of disturbed and undisturbed areas with labeled locations (a–f), where labels a–d indicate the locations of the four representative patches shown in Fig. 2.5. Panels (b) and (c) show false-color close-up views for locations e and f in panel (a), respectively. Each close-up covers an area of 100 m by 100 m.

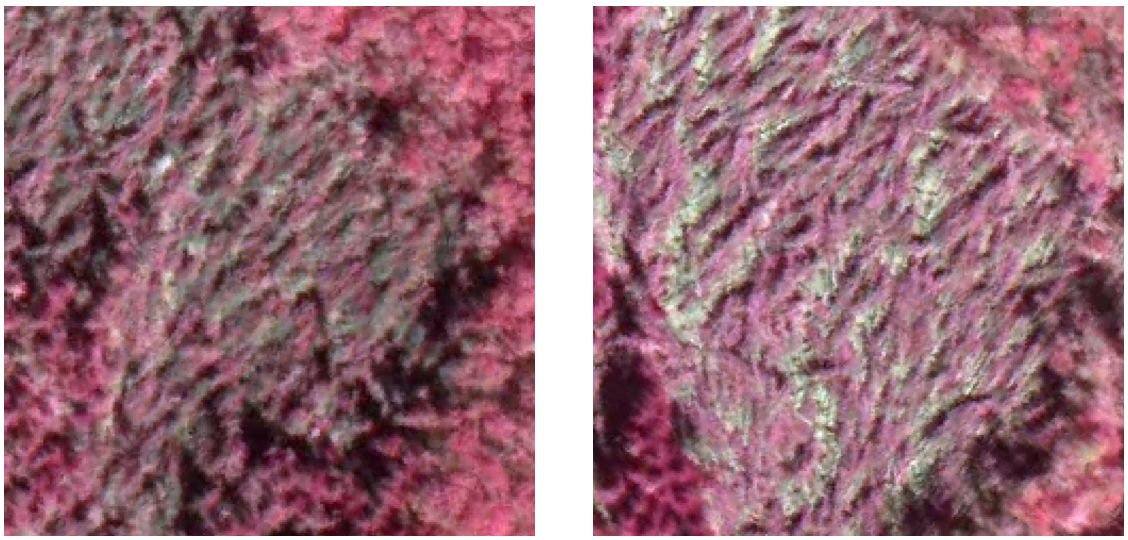

(b) (c)

Fig. 2.6. Continued: panels (b) and (c) show false-color close-up views for locations e and f.

For model training, the input data were processed into 256 × 256-pixel patches with a stride of 128 pixels. These patches, representing disturbed and undisturbed areas, were fed into a convolutional neural network (CNN) based on the ResNet-34 architecture (He et al., 2016). The key hyperparameters were set as follows: the learning rate was dynamically adjusted between 3.63×10^{-4} and 3.63×10^{-3}, with 20 training epochs and a batch size of 64. During the training process, the cross-entropy loss function was applied to optimize the model parameters. We applied data augmentation and early stopping to enhance generalization and prevent overfitting, following similar remote-sensing implementations (Gan et al., 2023; Mayra et al., 2021).

2.5 Needleleaf and broadleaf tree classification

We utilized high-resolution visible-light sensor data from a UAV in 2022 to map the distributions of needleleaf and broadleaf tree cover. We classified tree canopies into needleleaf and broadleaf categories using UAV imagery with a resolution of 6 cm. Both the UAV imagery and LiDAR data were acquired simultaneously in August 2022. Both datasets were directly georeferenced to the same coordinate reference system (CRS) without additional manual post-registration. Alignment quality was then checked by visual overlay inspection, and residual misalignment is acknowledged as a source of uncertainty. This concern is consistent with previous ALS-based inventory studies showing that co-registration error and edge effects can affect inventory accuracy (Pascual, 2019). The needleleaf–broadleaf classifier was trained using 256×256-pixel patches extracted with a stride of 128 pixels and a ResNet-34 backbone. The model was optimized using Adam with a cross-entropy loss function. The learning rate was dynamically adjusted between 3.63×10^{-4} and 3.63×10^{-3} over 20 epochs with a batch size of 64. Data augmentation included random crop, dihedral affine transforms, brightness adjustment, contrast adjustment, and zoom. Early stopping was enabled, and validation loss was used as the monitoring metric. UAV images for needleleaf (a) and broadleaf (b) forests are shown in Fig. 2.5(a) and Fig. 2.5(b). We did not employ the 2004 imagery for species classification because its relatively lower spatial resolution hindered reliable discrimination between needleleaf and broadleaf crowns. We specifically compared needleleaf and broadleaf stands because these two functional types often exhibit distinct morphological traits and physiological strategies, which can lead to different recovery trajectories following severe wind events (Mack et al., 2021).

The canopy height was estimated using LiDAR data collected by a UAV in 2022. We performed noise reduction on the raw LiDAR data and classified it into ground and nonground points. A digital terrain model (DTM) and a digital surface model (DSM) were generated on the basis of the average heights of the ground and nonground points, respectively. By subtracting ground elevation from the canopy surface, a 0.5 m CHM was produced. This 0.5 m CHM, derived from the 2022 UAV LiDAR data, was used only for individual-tree crown delineation (watershed segmentation) and crown polygon generation, and was not used for interannual AGB estimation.

The segmentation of individual trees was conducted using the watershed method (R package `lidR`) on the CHM. We first applied a 3×3-pixel window using a median filter to smooth the CHM. Although CHM-based individual tree segmentation algorithms are known to suffer from oversegmentation of complex broadleaf crowns and, conversely, undersegmentation of overlapping neighboring crowns (Yun et al., 2021), our use of CHM segmentation is confined to the binary task of distinguishing coniferous from broadleaf trees, so these biases are expected to have only a minimal impact on our results.

In this study, we manually labeled 1,347 trees, ensuring a representative distribution across the entire study area. Given that needleleaf trees were smaller and less abundant than broadleaf trees in the study area, we aimed to label an equal number of needleleaf and broadleaf trees to allow the model to learn balanced features for each category and prevent bias toward any one class. Subsequently, 90% of the labeled data were randomly selected as the training set, whereas 10% were used as the validation set. Following the same principle as the disturbance classifier, final needleleaf–broadleaf classification performance was evaluated using an independent spatially separated test set that was not split

from the original training/validation data. The input for classification consisted solely of the 6 cm ground sample distance (GSD) RGB UAV orthomosaic. Reference tree locations were represented by centroids of CHM-derived crown polygons, and we exported a fixed-size 256 × 256-pixel chip centered on each centroid (approximately 15 m on the ground) and center-cropped it to 224 × 224 px before training. This workflow targeted crown-type classification rather than stem-level ITD inventory construction; therefore, field-measured stem-base coordinates were not used as training targets in this step. We then employed a target classification method based on the ResNet34 architecture (He et al., 2016), using each tree and its surrounding pixels as inputs for the deep learning model, with labels for each tree (needleleaf = 1, broadleaf = 2) as the ground truth. Using this trained model, we classified all trees in the study area and generated a needleleaf–broadleaf individual tree-type distribution map.

2.6 Analysis of various impacts on the growth rate of aboveground forest biomass

The allometric equation was applied to the harmonized 2 m CHMs to derive AGB maps for the years 2004, 2014, and 2022. For each combination of disturbance status (disturbed and undisturbed), forest type (needleleaf and broadleaf), and interval (2004–2014, 2014–2022, and 2004–2022), we computed annualized CHM and AGB growth at 2 m grid-cell resolution.

3 Results

3.1 Classification accuracy assessment

The disturbance-classification model achieved an overall accuracy of 99.6% (Balanced Accuracy (BA) = 98.4%) on the validation set (Table 3.1). On the independent spatially separated test set, it achieved an overall accuracy of 95.7% and BA of 92.2% (Table 3.3). For the needleleaf–broadleaf classifier, the validation-set performance was 95.4% overall accuracy (BA = 95.3%; Table 3.2), whereas the independent test-set performance was 93.5% overall accuracy and 93.5% BA (Table 3.4). These results indicate that model performance remained high under spatially independent testing, although both classifiers showed expected accuracy reductions compared with validation-set results. The larger drop for disturbance classification (particularly BA) suggests stronger effects of spatial heterogeneity and class imbalance, whereas needleleaf–broadleaf classification remained comparatively stable.

Table 3.1. Confusion matrix of typhoon-disturbance classification on the validation set.

Confusion Matrix	Disturbed (ground truth)	Undisturbed (ground truth)
Classified as Disturbed	566	11
Classified as Undisturbed	18	5,855

Table 3.2. Confusion matrix of needleleaf–broadleaf forest classification on the validation set.

Confusion Matrix	Needleleaf (ground truth)	Broadleaf (ground truth)
Classified as Needleleaf	59 (TP)	1 (FP)
Classified as Broadleaf	5 (FN)	66 (TN)

Table 3.3. Confusion matrix of typhoon-disturbance classification on the independent test set. Overall accuracy = 95.7%, balanced accuracy = 92.2%.

Confusion Matrix	Disturbed (ground truth)	Undisturbed (ground truth)
Classified as Disturbed	735	178
Classified as Undisturbed	104	5,537

Table 3.4. Confusion matrix of needleleaf–broadleaf forest classification on the independent test set. Overall accuracy = 93.5%, balanced accuracy = 93.5%.

Confusion Matrix	Needleleaf (ground truth)	Broadleaf (ground truth)
Classified as Needleleaf	150	9
Classified as Broadleaf	12	150

3.2 Forest structure and disturbance patterns

Based on 2022 UAV imagery, the total forest area is 2,024.99 ha. Of this, 1,889.40 ha (93.3%) was classified as broadleaf forest, while 135.58 ha (6.7%) was classified as needle-leaf forest (Fig. 3.1). According to 2004 aerial imagery, undisturbed forest occupies 1,950.02 ha (96.3%), whereas disturbed areas cover 74.97 ha (3.7%).

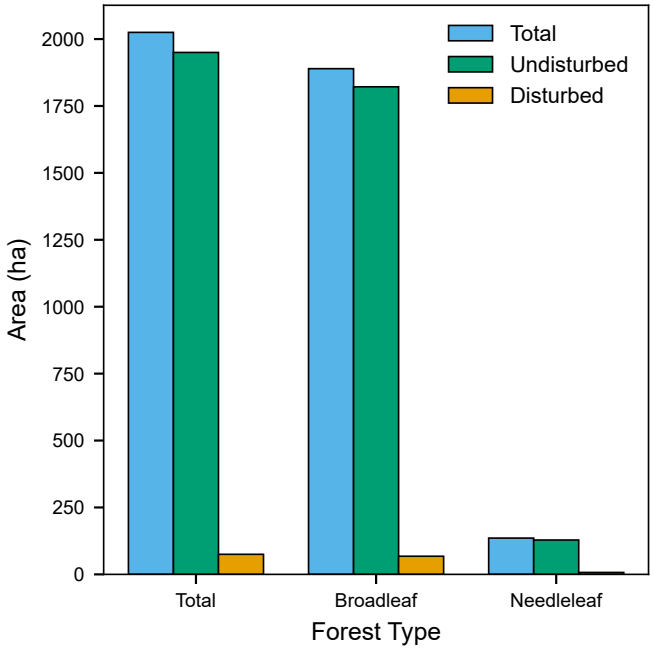

Fig. 3.1. Areas of total, disturbed, and undisturbed forests with tree types (broadleaf vs. needleleaf).

As shown in Fig. 3.2, derived from deep learning-based classification, disturbed and undisturbed forests as well as needleleaf and broadleaf forests are intermingled across the study region. As shown in Fig. 2.6(a), disturbed areas are mainly distributed as small,

spatially dispersed patches rather than as a single concentrated cluster.

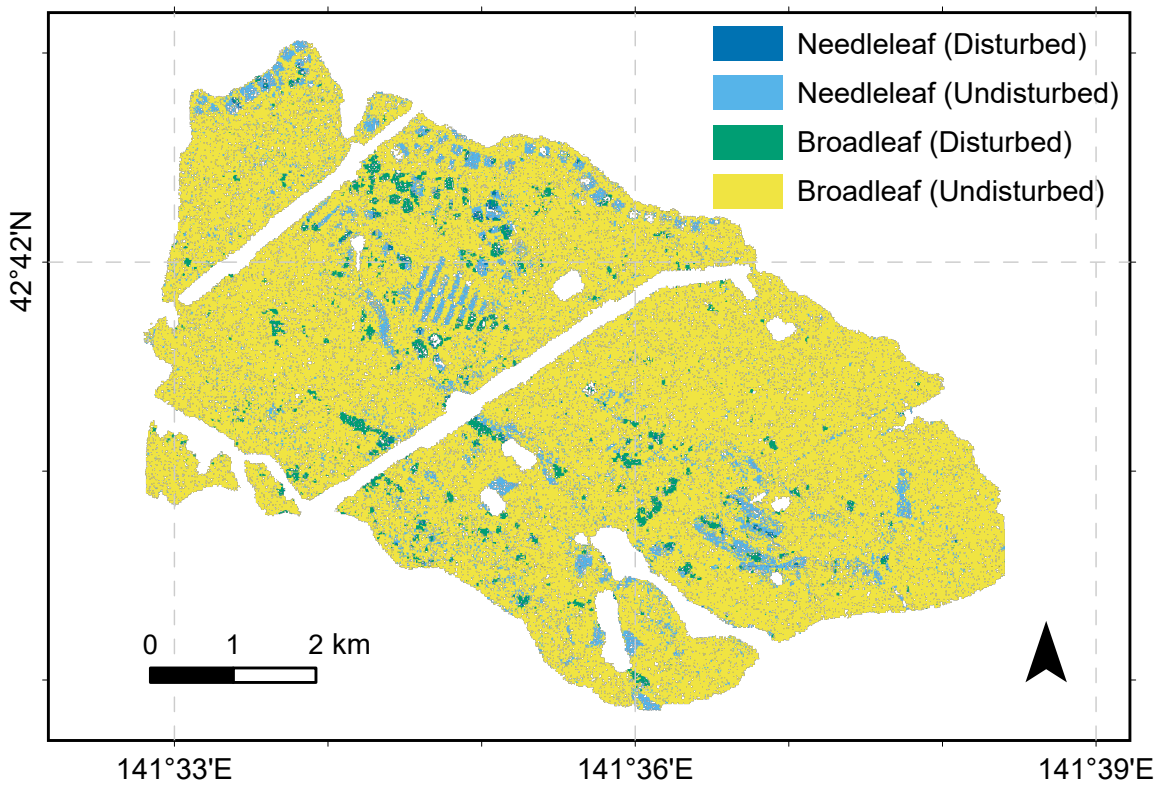

Fig. 3.2. Distributions of undisturbed vs. disturbed and needleleaf vs. broadleaf forests in the Tomakomai experimental forest of Hokkaido University.

3.3 Coupling of CHM and AGB, and the allometric growth effect

AGB was positively correlated with CHM (R^2 = 0.37; Fig. 3.3), where each 1 m increase in mean canopy height corresponds to an increase in AGB of approximately 9.76 Mg ha^{-1}.

The slope obtained here (9.76 Mg ha^{-1} m^{-1}) closely matches the 9.80 Mg ha^{-1} m^{-1} reported by Hojo et al. (2023) for a single-epoch LiDAR–CHM model in the same experimental forest. After harmonization, residual distributions grouped by LiDAR survey year showed substantial overlap and no clear systematic offset (Fig. 3.5), indicating that the normalized CHMs did not introduce a strong year-structured bias into the pooled calibration.

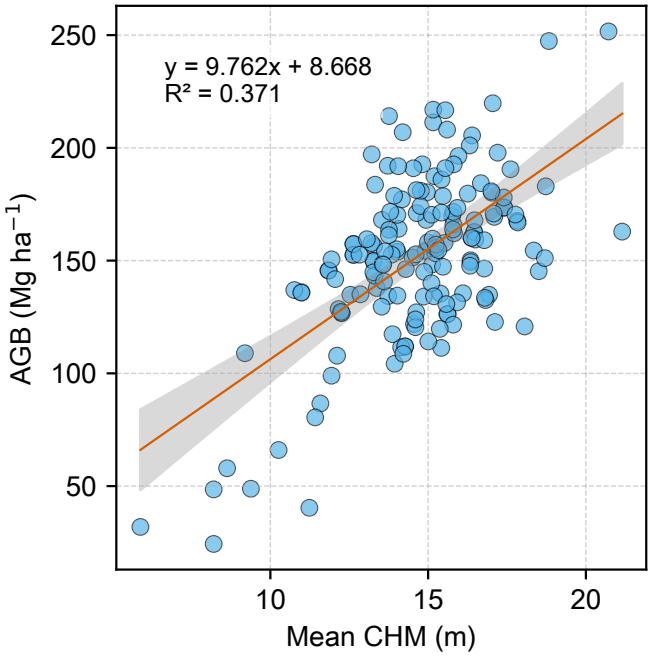

Fig. 3.3. Relationships between ground plot-measured AGB and the LiDAR-derived mean CHM. The scatter plot shows the linear regression line and 95% confidence interval for AGB (Mg ha^{-1}) as a function of the mean CHM (m). The regression is based on 165 plot-year observations from 114 unique RTK-surveyed field plots. Absolute RMSE and relative RMSE are 28.75 Mg ha^{-1} and 18.94%, respectively; the error-against-height-proxy relationship is shown in Fig. 3.4.

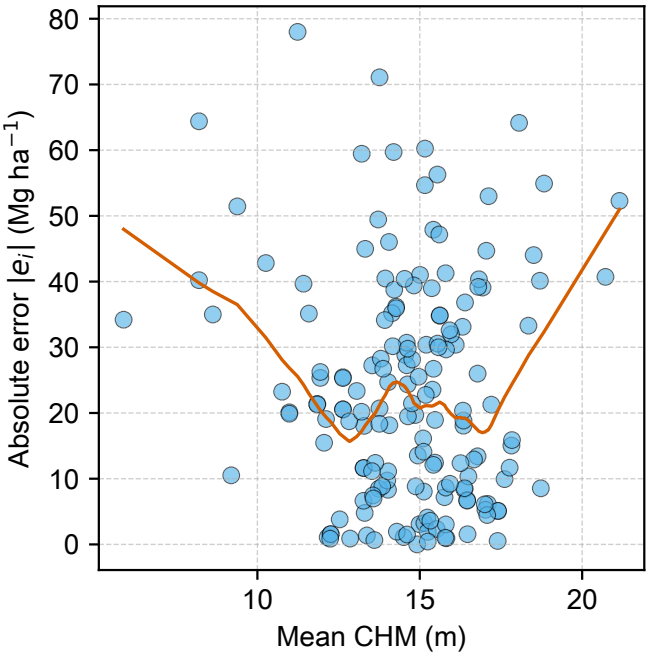

Fig. 3.4. Absolute residual error against mean CHM (used as a proxy for tree height) for the CHM–AGB regression. Each point shows $|e_i| = |AGB_{obs} - AGB_{pred}|$ (Mg ha^{-1}), and the orange curve indicates the LOWESS trend.

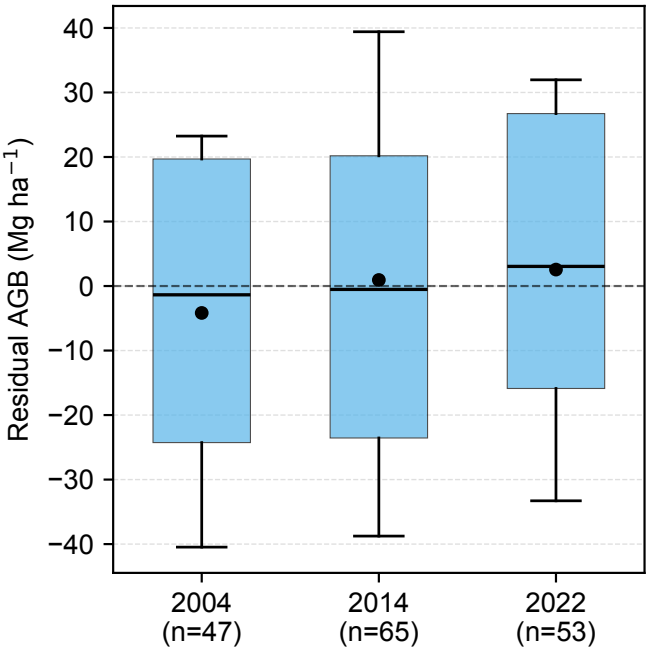

Fig. 3.5. Residual distributions of the pooled CHM–AGB calibration grouped by LiDAR survey year (2004, 2014, and 2022). Residuals are defined as observed minus predicted AGB (Mg ha^{-1}) from the pooled linear regression (Fig. 3.3). In each box-and-whisker plot, the center line represents the median, the box limits denote the 25th and 75th percentiles, the whiskers extend to the 10th and 90th percentiles, and the mean is shown by a dot. The dashed horizontal line indicates zero residual. Field observations were temporally matched to LiDAR survey years: 2002 and 2004 plots to the 2004 CHM, 2013 and 2014 plots to the 2014 CHM, and 2020 and 2021 plots to the 2022 CHM. Sample sizes (n) denote the number of plot-year observations in each group.

3.4 Dynamics of forest canopy height and AGB

The statistics in this subsection are reported at the 2 m grid-cell level (by disturbance status and forest type), rather than at the field-plot level. Disturbed stands showed slightly higher mean CHM and AGB growth than undisturbed stands, suggesting higher recovery potential after disturbance. Growth rates were lower during 2004–2014 and increased during 2014–2022, indicating delayed but substantial recovery. The delayed recovery signal is most evident in disturbed stands. In the CHM plots (Fig. 3.6 and Fig. 3.7), disturbed stands show broader distributions than undisturbed stands and a clear upward shift from 2004–2014 to 2014–2022, indicating greater structural heterogeneity during recovery. This delayed-recovery pattern is even more pronounced in the AGB plots (Fig. 3.10 and Fig. 3.11), where disturbed stands exhibit higher and more variable growth rates in the second interval, whereas undisturbed broadleaf stands show comparatively little temporal change (Tables 3.5–3.6).

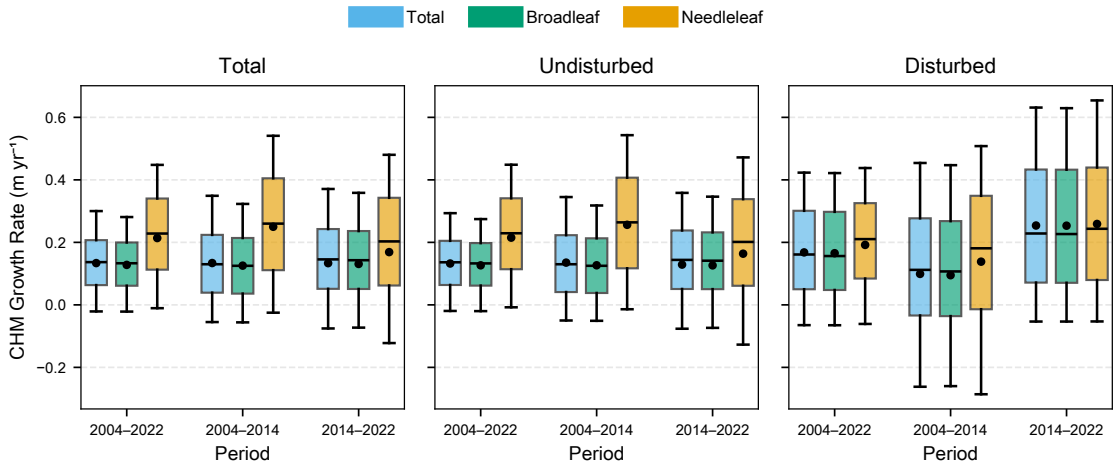

Fig. 3.6. Averaged annual growth rates of the forest canopy height model (CHM) across disturbance categories (total forest, undisturbed, and disturbed areas) over an 18-year period (2004–2022) of total, broadleaf, and needleleaf tree types. In the box-and-whisker plots, the center line represents the median, the box limits denote the 25th and 75th percentiles, the whiskers extend to the 10th and 90th percentiles, and the mean is shown by a dot. Growth rates are calculated based on a comparison of CHM values across 2004, 2014, and 2022, with disturbance areas and tree types identified using aerial imagery and classification models.

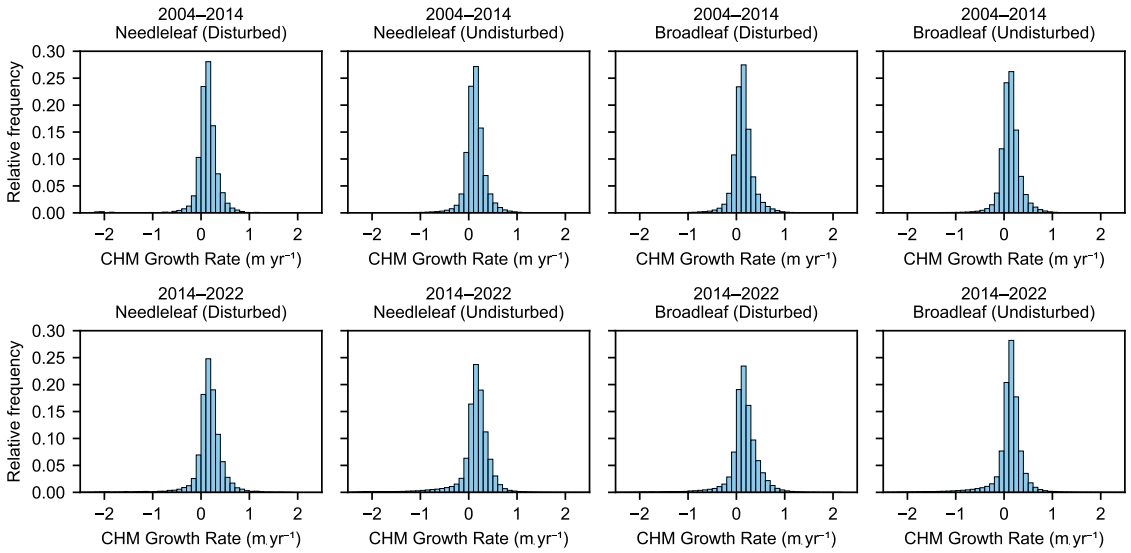

Fig. 3.7. Distributions of canopy height growth rates for disturbed and undisturbed needleleaf and broadleaf forests during 2004–2014 and 2014–2022. Histograms of annual CHM growth rates (m yr^{-1}) derived from LiDAR data for needleleaf and broadleaf stands under disturbed and undisturbed conditions across two intervals (2004–2014: top panels; 2014–2022: bottom panels). Each column corresponds to a forest category (needleleaf disturbed, needleleaf undisturbed, broadleaf disturbed, broadleaf undisturbed). The horizontal axis indicates the CHM growth rate (m yr^{-1}), and the vertical axis indicates the relative frequency of the pixels.

Table 3.5. Decadal variation in forest canopy height growth rates across disturbance categories. This table presents the mean ± standard deviation, median, and 10th–90th percentile range (P10 to P90) of the CHM growth rates (m yr^{-1}) collected over an 18-year period (2004–2022) and derived from airborne LiDAR data. The growth rates are reported for the total forest, undisturbed areas, and disturbed areas, which are further categorized by total, broadleaf, and needleleaf tree types. Growth rates are calculated on the basis of a comparison of CHM values across 2004, 2014, and 2022, with disturbance areas identified using aerial imagery and classification models.

Period		CHM growth rate (m yr^{-1}) Mean ± SD (Median; P10 to P90)		
		Total	Broadleaf	Needleleaf
Total	2004–2022	0.13 ± 0.16 (0.14; -0.02 to 0.30)	0.13 ± 0.15 (0.13; -0.02 to 0.28)	0.21 ± 0.21 (0.23; -0.01 to 0.45)
Total	2004–2014	0.13 ± 0.21 (0.13; -0.05 to 0.35)	0.13 ± 0.21 (0.12; -0.06 to 0.32)	0.25 ± 0.27 (0.26; -0.02 to 0.54)
Total	2014–2022	0.13 ± 0.28 (0.15; -0.08 to 0.37)	0.13 ± 0.27 (0.14; -0.07 to 0.36)	0.17 ± 0.35 (0.20; -0.12 to 0.48)
Undisturbed	2004–2022	0.13 ± 0.16 (0.14; -0.02 to 0.29)	0.13 ± 0.15 (0.13; -0.02 to 0.27)	0.22 ± 0.21 (0.23; -0.01 to 0.45)
Undisturbed	2004–2014	0.14 ± 0.21 (0.13; -0.05 to 0.34)	0.13 ± 0.21 (0.12; -0.05 to 0.32)	0.26 ± 0.27 (0.26; -0.01 to 0.54)
Undisturbed	2014–2022	0.13 ± 0.28 (0.14; -0.08 to 0.36)	0.13 ± 0.27 (0.14; -0.07 to 0.35)	0.26 ± 0.35 (0.26; -0.13 to 0.47)

Table 3.5. Continued

Period		CHM growth rate (m yr^{-1}) Mean ± SD (Median; P10 to P90)		
		Total	Broadleaf	Needleleaf
Disturbed	2004–2022	0.17 ± 0.20 (0.16; -0.06 to 0.42)	0.17 ± 0.20 (0.16; -0.07 to 0.42)	0.19 ± 0.21 (0.21; 0.06 to 0.44)
Disturbed	2004–2014	0.10 ± 0.32 (0.11; -0.26 to 0.45)	0.09 ± 0.32 (0.08; -0.32 to 0.45)	0.14 ± 0.35 (0.18; -0.29 to 0.51)
Disturbed	2014–2022	0.25 ± 0.31 (0.23; -0.05 to 0.63)	0.25 ± 0.31 (0.23; -0.05 to 0.63)	0.26 ± 0.35 (0.26; -0.04 to 0.65)

Table 3.6. Aboveground biomass (AGB) growth rates under different conditions. This table presents the mean ± standard deviation, median, and 10th–90th percentile range (P10 to P90) of AGB growth rates (Mg ha^{-1} yr^{-1}; dry weight) for total, broadleaf, and needleleaf stands from 2004 to 2022, based on airborne LiDAR measurements in the Tomakomai Experimental Forest, Hokkaido, Japan. "Total" represents the entire study area, "Undisturbed" denotes areas not affected by typhoons, and "Disturbed" indicates areas subjected to typhoon disturbances. Periods correspond to 2004–2022 (full study duration), 2004–2014 (first interval), and 2014–2022 (second interval).

Period		AGB growth rate (Mg ha^{-1} yr^{-1}) Mean ± SD (Median; P10 to P90)		
		Total	Broadleaf	Needleleaf
Total	2004–2022	1.30 ± 1.55 (1.34; -0.20 to 2.93)	1.25 ± 1.50 (1.30; -0.21 to 2.74)	2.09 ± 2.02 (2.23; -0.10 to 4.37)
Total	2004–2014	1.31 ± 2.08 (1.27; -0.54 to 3.41)	1.23 ± 2.00 (1.22; -0.55 to 3.15)	2.44 ± 2.66 (2.54; -0.24 to 5.28)
Total	2014–2022	1.30 ± 2.71 (1.42; -0.74 to 3.62)	1.28 ± 2.65 (1.39; -0.71 to 3.50)	1.65 ± 3.43 (1.98; -1.19 to 4.69)
Undisturbed	2004–2022	1.29 ± 1.53 (1.33; -0.19 to 2.86)	1.24 ± 1.48 (1.30; -0.21 to 2.68)	2.10 ± 2.01 (2.24; -0.08 to 4.38)
Undisturbed	2004–2014	1.32 ± 2.03 (1.27; -0.49 to 3.37)	1.24 ± 1.95 (1.22; -0.50 to 3.10)	2.50 ± 2.59 (2.58; -0.14 to 5.30)
Undisturbed	2014–2022	1.26 ± 2.69 (1.40; -0.75 to 3.50)	1.23 ± 2.63 (1.38; -0.72 to 3.38)	1.60 ± 3.42 (1.97; -1.24 to 4.61)

Table 3.6. Continued

Period		AGB growth rate (Mg ha^{-1} yr^{-1}) Mean ± SD (Median; P10 to P90)		
		Total	Broadleaf	Needleleaf
Disturbed	2004–2022	1.64 ± 1.96 (1.57; -0.63 to 4.13)	1.61 ± 1.95 (1.53; -0.64 to 4.12)	1.87 ± 2.08 (2.05; -0.06 to 4.27)
Disturbed	2004–2014	0.97 ± 3.12 (1.09; -2.56 to 4.43)	0.84 ± 3.08 (1.04; -2.54 to 4.36)	1.35 ± 3.45 (1.77; -2.79 to 4.96)
Disturbed	2014–2022	2.48 ± 3.06 (2.23; -0.52 to 6.16)	2.47 ± 3.02 (2.21; -0.52 to 6.14)	2.84 ± 3.67 (2.38; -0.52 to 6.39)

DTM distributions were broadly comparable across 2004, 2014, and 2022 (Fig. 3.8). Difference maps and summary statistics against 2004 (Fig. 3.9 and Table 3.7) indicate localized differences, with greater variability in $DTM_{2022} - DTM_{2004}$ than in $DTM_{2014} - DTM_{2004}$, as indicated by higher RMSE and a wider P5–P95 range. These localized differences may partly reflect acquisition-related effects, including differences in pulse penetration and ground-return sampling between UAV and ALS LiDAR, as well as possible real surface changes (Badouard et al., 2025).

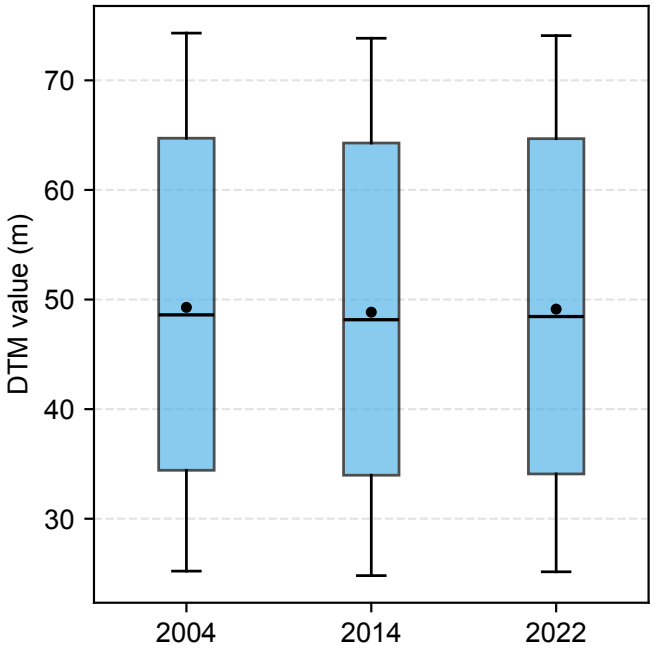

Fig. 3.8. Cross-year comparison of DTM distributions (2004, 2014, and 2022) in the overlapping analysis domain. Boxplots summarize terrain-surface consistency across survey years.

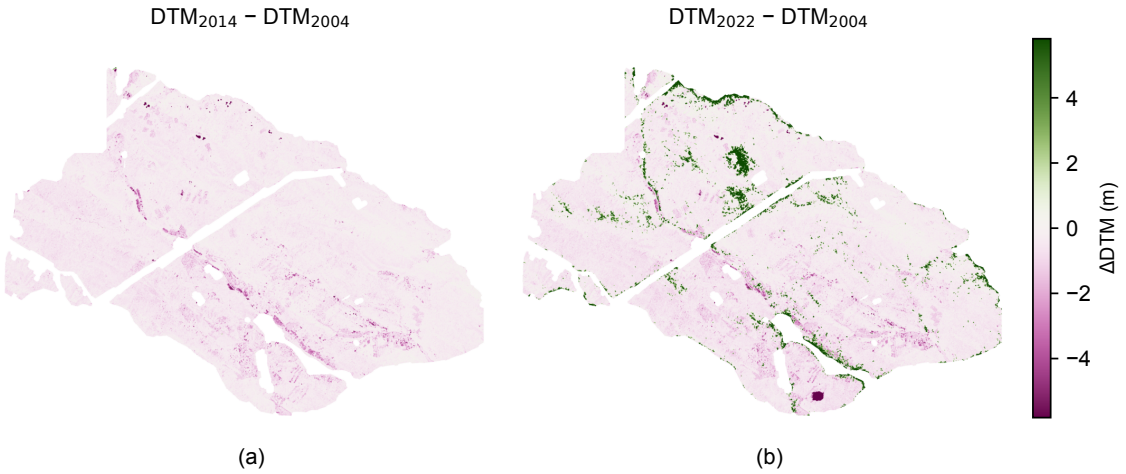

Fig. 3.9. Spatial DTM difference maps against 2004: (a) $DTM_{2014} - DTM_{2004}$ and (b) $DTM_{2022} - DTM_{2004}$.

Table 3.7. Summary statistics for DTM comparability against 2004. Mean bias, median, RMSE, and percentile ranges are reported for $DTM_{2014} - DTM_{2004}$ and $DTM_{2022} - DTM_{2004}$.

Pair	Mean bias (m)	Median (m)	RMSE (m)	P5 (m)	P95 (m)	N cells
$DTM_{2014} - DTM_{2004}$	-0.4382	-0.3900	0.6850	-1.1200	0.1600	5,646,823
$DTM_{2022} - DTM_{2004}$	-0.1594	-0.3699	1.6199	-1.1677	1.0551	5,647,163

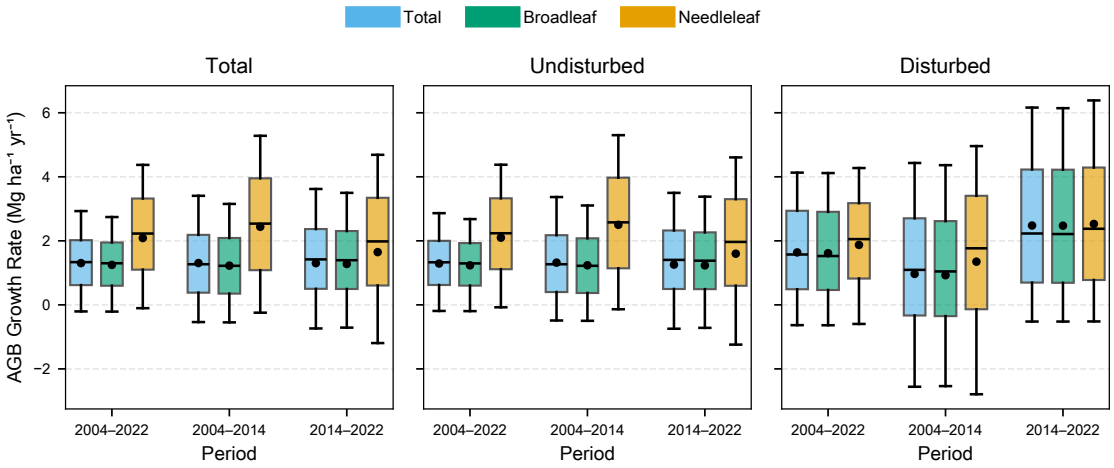

Fig. 3.10. AGB growth rates across disturbance categories (total forest, undisturbed, and disturbed areas) over an 18-year period (2004–2022) of total, broadleaf, and needleleaf tree types. In the box-and-whisker plots, the center line represents the median, the box limits denote the 25th and 75th percentiles, the whiskers extend to the 10th and 90th percentiles, and the mean is shown by a dot. "Total" represents the entire study area, "Undisturbed" denotes areas that have not been identified as having typhoon-induced windthrow, and "Disturbed" indicates areas identified with typhoon-induced windthrow. Periods correspond to 2004–2022 (full study duration), 2004–2014 (first interval), and 2014–2022 (second interval). Sample sizes (n) for all Fig. 3.10 boxplots are provided in Table 3.8; n denotes the number of 2-m grid cells in each period × disturbance-status × tree-type subgroup.

Table 3.8. Sample sizes (n) for Fig. 3.10 boxplots by period, disturbance status, and tree type. Here, n denotes the number of 2-m grid cells in each subgroup. For a given subgroup, n is identical across periods because growth rates for all periods were computed on the same valid classified pixel footprint.

	Period	Sample size, n (2 m grid cells)		
		Total	Broadleaf	Needleleaf
Total	2004–2022	5,062,473	4,723,511	338,962
Total	2004–2014	5,062,473	4,723,511	338,962
Total	2014–2022	5,062,473	4,723,511	338,962
Undisturbed	2004–2022	4,875,044	4,554,082	320,962
Undisturbed	2004–2014	4,875,044	4,554,082	320,962
Undisturbed	2014–2022	4,875,044	4,554,082	320,962
Disturbed	2004–2022	187,429	169,429	18,000
Disturbed	2004–2014	187,429	169,429	18,000
Disturbed	2014–2022	187,429	169,429	18,000

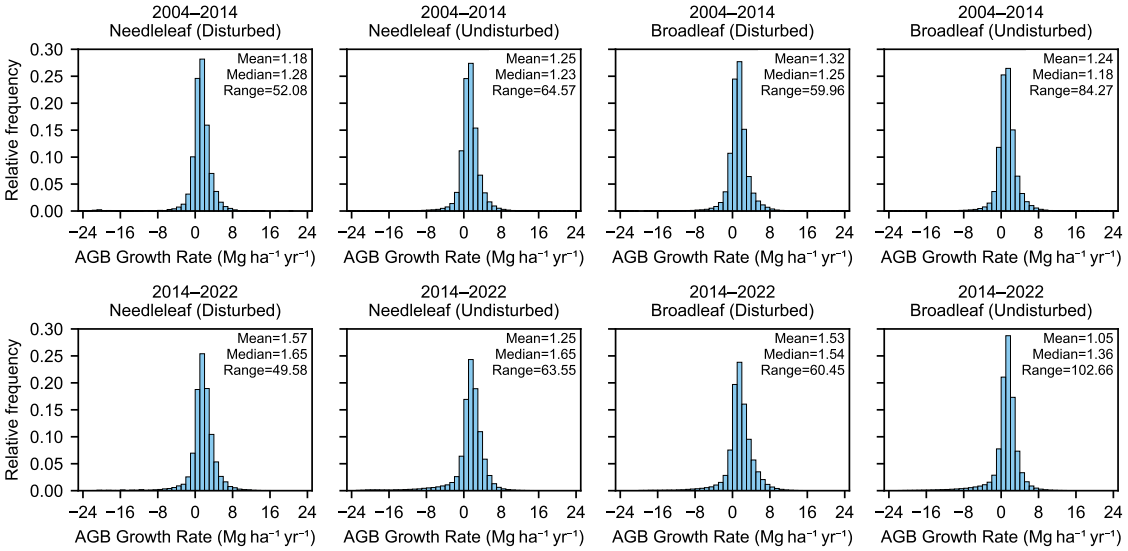

Fig. 3.11. Distributions of AGB growth rates for disturbed and undisturbed needleleaf and broadleaf forests during 2004–2014 and 2014–2022. Histograms of annual AGB growth rates (Mg ha^{-1} yr^{-1}) derived from LiDAR data for needleleaf and broadleaf stands under disturbed and undisturbed conditions across two intervals (2004–2014: top panels; 2014–2022: bottom panels). Each column corresponds to a forest category (needleleaf disturbed, needleleaf undisturbed, broadleaf disturbed, broadleaf undisturbed). The horizontal axis indicates the AGB growth rate, and the vertical axis indicates the relative frequency of the pixels. Mean, median, and range are annotated in each histogram panel. Quantile–quantile comparisons between the two intervals for the same classes are provided in Fig. 3.12.

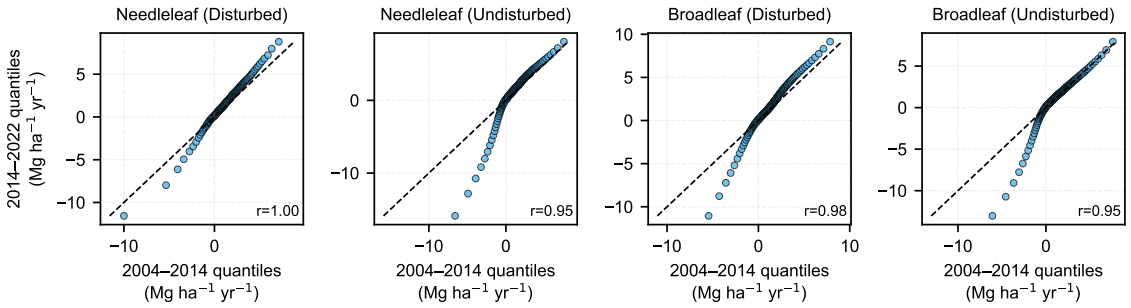

Fig. 3.12. Quantile–quantile (Q–Q) comparison of AGB growth-rate distributions between 2004–2014 (x-axis) and 2014–2022 (y-axis) for four classes (needleleaf-disturbed, needleleaf-undisturbed, broadleaf-disturbed, and broadleaf-undisturbed). The dashed line indicates the 1:1 reference line.

Fig. 3.13 and Fig. 3.14 present the CHM and AGB trends for 2004, 2014, and 2022. The mean CHM across all stands increased from 12.46±3.85 m in 2004 to 14.86±3.37 m in 2022, while the corresponding mean AGB rose from 130.3 ± 37.6 Mg ha^{-1} to 153.7 ± 32.9 Mg ha^{-1}. Undisturbed areas increased from 12.64 ± 3.67 m to 15.02 ± 3.24 m in CHM, and from 132.1 ± 35.8 Mg ha^{-1} to 155.3 ± 31.6 Mg ha^{-1} in AGB, indicating that mature stands continue to heighten slowly while steadily accumulating biomass. In contrast, disturbed stands had a mean CHM of only 7.82 ± 5.14 m in 2004, which rose significantly to 10.84 ± 4.16 m in 2022; their mean AGB climbed in parallel from 85.0 ± 50.2 Mg ha^{-1} to 114.5 ± 40.6 Mg ha^{-1}.

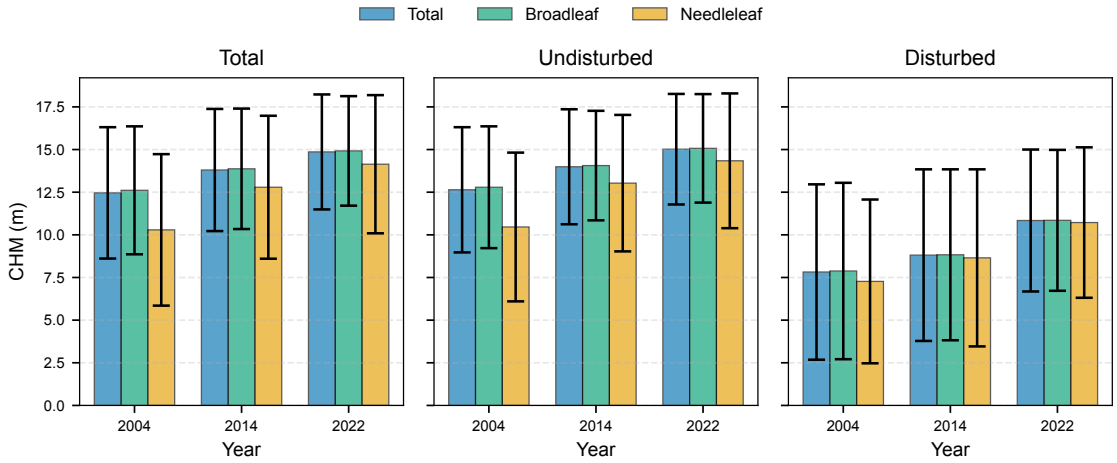

Fig. 3.13. Mean CHM by disturbance status, tree type, and year. This figure presents the mean CHM values for the Tomakomai Experimental Forest, categorized by disturbance status (disturbed vs. undisturbed) and tree type (broadleaf vs. needleleaf) for the years 2004, 2014, and 2022. The figure shows the mean CHM values with associated standard deviations.

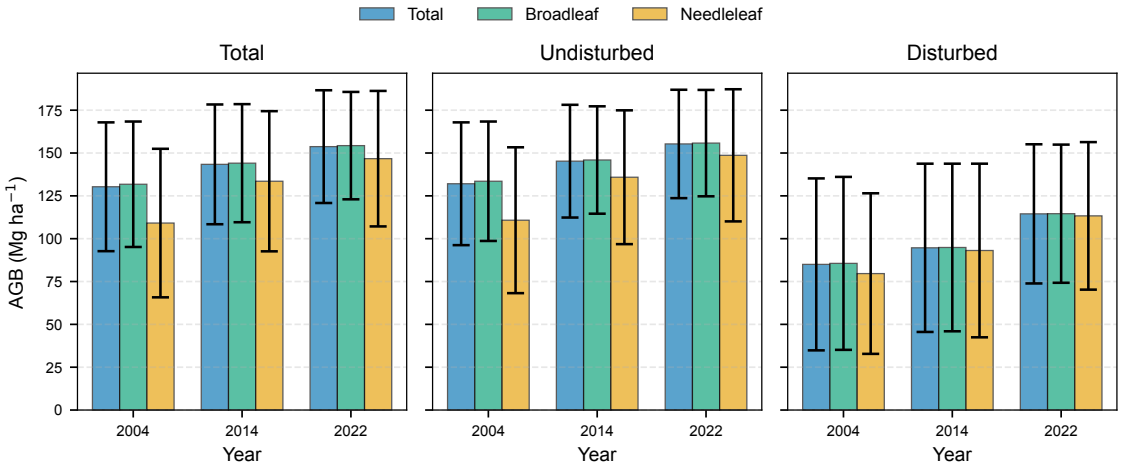

Fig. 3.14. Mean AGB by disturbance status, tree type, and year. This figure presents the mean AGB values for the Tomakomai Experimental Forest, categorized by disturbance status (disturbed vs. undisturbed) and tree type (broadleaf vs. needleleaf) for the years 2004, 2014, and 2022.

From 2004 to 2022, AGB increased across most of the region (Fig. 3.15a–c), and the net change map (Fig. 3.15d) shows predominantly positive ΔAGB across the landscape. Growth rates were spatially variable in both intervals (Fig. 3.16b–c), and the ΔAGR map (Fig. 3.16d) indicates a mixed pattern of acceleration and deceleration rather than a uniform landscape-wide shift. A small proportion of areas flanking roads and power lines showed negative AGB growth during the second interval, most likely because of tree harvesting.

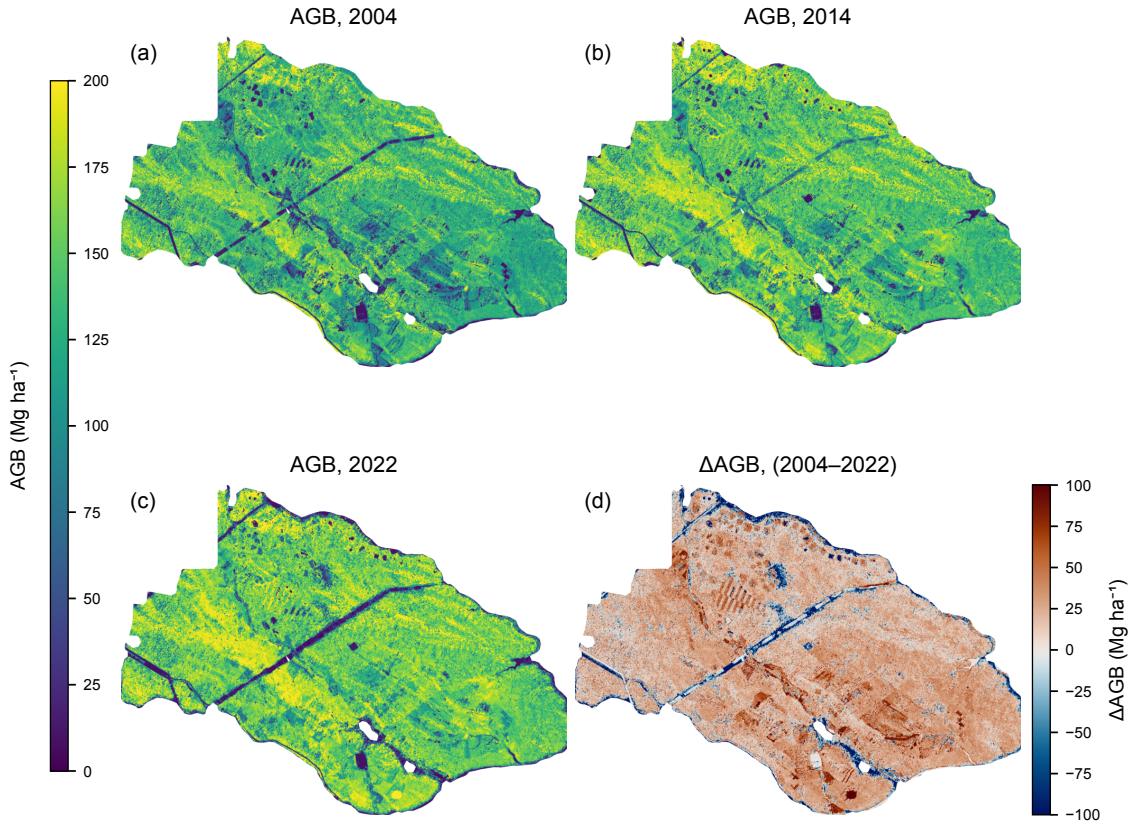

Fig. 3.15. Spatial distribution of LiDAR-derived AGB in the Tomakomai Experimental Forest for three survey years and the net 18-year change. (a) AGB in 2004, soon after Typhoon Songda; (b) AGB in 2014; (c) AGB in 2022; and (d) net change in AGB between 2004 and 2022 (ΔAGB). The left-hand color bar (panels a–c) expresses biomass density in Mg ha^{-1}, while the right-hand color bar shows the net change in AGB in Mg ha^{-1}, where negative values indicate loss and positive values indicate gain.

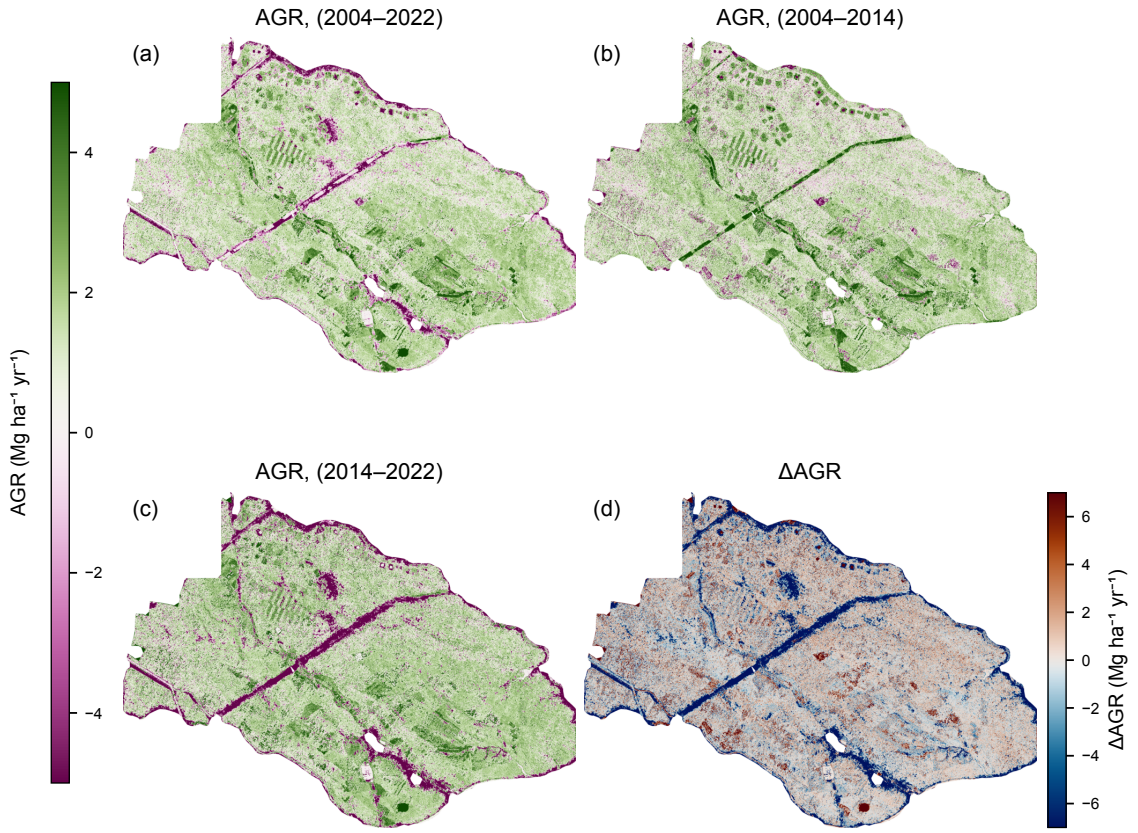

Fig. 3.16. Spatial distribution of the LiDAR-derived average growth rate (AGR, Mg ha^{-1} yr^{-1}) for AGB in the Tomakomai Experimental Forest for three observation windows and their temporal difference. (a) AGR over the full 18-year period (2004–2022); (b) AGR for interval 1 (2004–2014); (c) AGR for interval 2 (2014–2022); and (d) ΔAGR is the difference in AGR between interval 2 and interval 1. The color bar on the left (panels a–c) expresses AGR in Mg ha^{-1} yr^{-1}, where positive values indicate biomass gain and negative values indicate loss. The color bar on the right (panel d) represents ΔAGR in the same units, with positive values denoting an acceleration of biomass accumulation and negative values denoting a slowdown.

During both intervals (2004–2014 and 2014–2022; see Fig. 3.10 and Fig. 3.11), the annual AGB growth rate distributions differed significantly between needleleaf and broadleaf stands and between disturbed and undisturbed zones. In undisturbed areas, needleleaf forests consistently exhibited higher and more dispersed growth rates than their broadleaf counterparts. The growth rate of broadleaf stands remained generally stable between the two intervals, whereas the growth rate of needleleaf stands declined substantially in the second interval. Although severe windthrow did not occur in the undisturbed zone, typhoons may still cause partial crown breakage of standing needleleaf trees during the first interval; therefore, these stands were likely in a recovery phase and grew faster. By the second interval, most needleleaf stands had largely recovered, causing the median growth rate to decline. During this interval, the mean fell below the median, indicating a left-skewed distribution. Combined with patches showing negative AGB growth (Fig. 3.16), the evidence indicates selective logging.

The disturbed stands exhibited more dispersed AGB growth rate distributions than the undisturbed stands in both needleleaf and broadleaf forests, underlining the heightened growth heterogeneity that accompanies post-disturbance recovery. During the second interval (2014–2022) both forest types grew faster than in the first interval (2004–2014), implying a temporal lag before the main recovery phase becomes detectable. In the first interval, needleleaf stands outpaced broadleaf stands, yet their mean growth rate lay below the median, a left-skewed pattern that likely reflects salvage logging of wind-damaged conifers immediately after the typhoon. Within disturbed stands, by the second interval, growth rates and their distributions had largely converged between needleleaf and broadleaf forests. The mean slightly exceeded the median and the upper whisker extended further than the lower one, suggesting the emergence of a subset of fast-growing pioneer individuals in both forest

types (Pugh et al., 2019). Q–Q plots (Fig. 3.12) compare the 2004–2014 and 2014–2022 distributions within each class. They show reasonable agreement in the central quantiles, with systematic tail deviations from the 1:1 line. These within-class, cross-interval patterns are complementary to the between-class comparisons in Fig. 3.10. Upper-tail departures are generally larger in disturbed classes, suggesting relatively faster second-interval gains among high-growth pixels. Lower-to-middle quantile deviations may be associated with localized anthropogenic disturbances (e.g., selective logging), although logging intensity by period was not directly quantified in this study.

4 Discussion

4.1 Estimation of AGB growth from multiple airborne LiDAR data

The substantial variability in post-disturbance AGB recovery rates across tropical or subtropical forests underscores the importance of climate in shaping growth responses. In a neotropical context, Poorter et al. (2016) reported approximately 3.05 Mg C ha^{-1} yr^{-1} for early-stage secondary forests. Moreover, Requena Suarez et al. (2023) described post-disturbance recoveries of up to 6–7 Mg ha^{-1} yr^{-1} in the Amazon, driven by prolific gap dynamics following windthrows. Additionally, Requena Suarez et al. (2019) reinforced the notion that young tropical stands (20 years or less) can surpass 5 Mg ha^{-1} yr^{-1}.

In temperate climates, Geng et al. (2021) reported pre-disturbance increases near 2.46 Mg ha^{-1} yr^{-1} in selectively harvested forests in northeastern China, with post-harvest rates ranging from 1.17 to 2.46 Mg ha^{-1} yr^{-1}. Focusing on our cool-temperate forest in northern Japan, prior work by Hiura (2005) in the same Hokkaido landscape (pre-disturbance, 1981–1999) reported an average net biomass increase of approximately 1.66 Mg ha^{-1} yr^{-1} (dry weight; converted from 0.83 Mg C ha^{-1} yr^{-1}, assuming 50% carbon content). Relative to Hiura (2005)'s pre-disturbance baseline, our forest displayed slower initial growth in the first decade but subsequently accelerated.

4.2 Effects of Typhoon disturbance on the AGB growth rate in affected forests

Our findings indicate a marked time lag in the positive effects of natural events such as typhoon disturbances on temperate forest biomass and structure. In the first interval, the lower stand-level growth rates may partly reflect the early establishment phase of regenerating trees, whose height development typically follows a sigmoidal trajectory with initially limited growth that accelerates as trees increase in stature (Riofrío et al., 2023). Moreover, typhoon disturbances lowered the leaf area index (LAI) and consequently reduced carbon assimilation (Lian et al., 2024). In the second interval, a closing canopy while maintaining a higher gap fraction than in undisturbed stands likely accelerated growth. Likewise, a European study shows that, depending on disturbance severity, forests usually need 5.5–13.4 years to re-establish a closed canopy (Mandl et al., 2024). In addition to these stand-structural recovery processes, broader environmental changes over the study period may also have contributed to the higher AGB growth observed in 2014–2022. In particular, warmer conditions and increasing atmospheric CO_2 concentrations may have been additional contributing factors, although these effects were not directly quantified in this study and should therefore be interpreted as plausible background influences rather than demonstrated causal mechanisms (Anderson-Teixeira et al., 2013; Hirata et al., 2014; Walker et al., 2019).

Fig. 3.10 shows that in both undisturbed stands and stands within the first 10 years after disturbance, needleleaf trees grow faster than broadleaf trees. Earlier studies suggest this is because the broadleaf trees in the study area are mainly natural forests, whereas the

needleleaf trees are mostly plantations. The needleleaf trees are generally younger than the broadleaf trees and therefore exhibit higher growth rates (Hiura, 2005).

Fig. 3.3 shows a positive correlation between CHM and AGB; however, the R^2 value (~0.37) indicates that canopy height is only one of many factors influencing AGB. The height–biomass relationship is constrained by multiple variables, including crown size and wood density (Jucker et al., 2017). Future approaches that integrate ground inventory data, or 3D structural metrics (such as voxel-based LiDAR methods) could improve the robustness and accuracy of AGB estimates (Pimont et al., 2018).

The findings of this study offer multiple insights for managers and policy-makers. First, disturbed forests may not exhibit substantial accelerated growth and increases in carbon sinks until approximately a decade after disturbance, implying that short-term monitoring alone is insufficient to capture the full impact. Second, needleleaf forests showed higher mean AGB growth rates than broadleaved forests over the 18 year study period, providing valuable guidance for afforestation and restoration strategies. Third, in structurally heterogeneous forests, management that enhances resilience and optimizes stand structure may help maintain carbon sequestration capacity (Wolf and Paul-Limoges, 2023).

4.3 Study limitations and future directions

One limitation of this study is the absence of pre-disturbance (pre-2004) imagery or records, which prevents distinguishing whether current broadleaf stands already existed before 2004

or emerged through conifer-to-broadleaf conversion after the typhoon. Previous studies in the Tomakomai region reported heavier typhoon damage in conifer plantations, especially Japanese larch (Hayashi et al., 2015; Sano et al., 2010; Takahashi et al., 2011). However, regional or site-level evidence cannot replace pre- and post-typhoon, species-resolved, individually matched tree records within our study area, which were unavailable in this study. Research in similar forests suggests that severe windthrow events can facilitate such transitions from needleleaf dominance to broadleaf dominance (Wu et al., 2019). Another related uncertainty involves attributing all observed treefalls in 2004 to typhoon damage; it is possible that some mortality occurred before the storm. However, the consistent direction of fallen stems, coupled with windthrow pattern reports (Hayashi et al., 2015; Wu et al., 2019), supports the conclusion that most cases were typhoon-induced. Incorporating pre-typhoon baseline references in future studies would help more conclusively identify whether the observed changes arose from the 2004 disturbance or earlier processes.

A second major limitation is related to the spatial resolution gap between the 2004 aerial photographs and the higher-resolution UAV data from 2022. The 2004 photos were sufficiently coarse that only fully toppled trees could be reliably identified as "disturbed," whereas partially damaged or leaning trees likely remained indistinguishable from the intact canopy and were thus misclassified as "undisturbed." A similar underestimation of wind damage has been noted in other studies using coarser satellite or aerial imagery (Negrón-Juárez et al., 2010). Post-2022 aerial imagery was unavailable in this study area, so direct image-based verification of post-2022 CHM change could not be performed. Therefore, changes in CHM and AGB were interpreted conservatively, and DTM comparability diagnostics (Fig. 3.8, Fig. 3.9, and Table 3.7) were used as indirect quality checks against potential artifacts.

Finally, this study does not account for small-scale anthropogenic disturbances—such as unrecorded selective logging near roads—that may have occurred during the study period. According to our histograms, a small fraction of pixels exhibited negative biomass changes, suggesting that some losses might stem from such unmonitored interventions (Fig. 3.11). Without detailed logging records or management plans, disentangling human-driven biomass removal from natural processes (such as mortality) or data-related errors is difficult (Asner et al., 2005; Hethcoat et al., 2019). Future efforts should incorporate fine-scale forest management data and harvest maps to better attribute localized reductions in biomass. Because calibration was performed at the plot level while mapping was conducted at 2 m grid-cell resolution, scale-transfer uncertainty may remain. To mitigate this issue, the key inferences of this study are primarily based on aggregated statistics rather than single-pixel interpretation.

As an external context, GEDI L4A AGBD was summarized within the study boundary. Because valid coverage was highly uneven across years, GEDI results were used as contextual evidence only and were not used for robust interannual trend inference in this study (Table 4.1).

Table 4.1. Annual GEDI L4A AGBD summary statistics within the study boundary (2019–2024), calculated for growing-season months (May–October) after quality filtering (l4_quality_flag = 1 and degrade_flag = 0). Years with no valid pixels are reported as NA. *n* denotes the number of valid GEDI pixels within the study boundary after filtering.

Year	*n*	AGBD mean (Mg ha^{-1})	AGBD stdDev (Mg ha^{-1})
2019	1	85.66	0.00
2020	0	NA	NA
2021	846	132.36	44.55
2022	0	NA	NA
2023	0	NA	NA
2024	0	NA	NA

5 Conclusion

By integrating multitemporal LiDAR datasets, deep-learning-based disturbance and tree-type classifications, and field measurements within one harmonized cross-year framework, this dissertation quantified post-typhoon forest recovery in the Tomakomai Experimental Forest at 2 m grid-cell resolution. The study combined three LiDAR surveys from 2004, 2014, and 2022 with temporally matched plot data to calibrate a CHM–AGB relationship and to generate year-specific maps of canopy height and aboveground biomass (AGB; dry weight). This design enabled more consistent long-term comparisons after Typhoon Songda by reducing confounding from inconsistent spatial resolution or processing scale.

At the whole-forest scale, mean CHM increased from 12.46 m in 2004 to 14.86 m in 2022, and mean AGB increased from 130.3 to 153.7 Mg ha^{-1}, corresponding to an annualized AGB increase of 1.30 Mg ha^{-1} yr^{-1}. Disturbed stands showed faster biomass recovery than undisturbed stands over the full 18-year period (1.64 vs. 1.29 Mg ha^{-1} yr^{-1}). Within disturbed stands, AGB growth accelerated markedly from 0.97 Mg ha^{-1} yr^{-1} during 2004–2014 to 2.48 Mg ha^{-1} yr^{-1} during 2014–2022. These results indicate that the main recovery response was not immediate after the typhoon, but emerged after a substantial lag, with persistent spatial heterogeneity between disturbance classes and between needleleaf and broadleaf stands.

Ecologically, these findings show that severe wind disturbance in a broadleaf-dominated

cool-temperate forest can be followed by substantial biomass recovery, but that recovery is delayed rather than instantaneous. The contrast between the early post-disturbance interval and the later accelerated phase suggests that canopy reorganization, stand redevelopment, and the emergence of fast-growing individuals together shape recovery trajectories. The results also imply that short-term assessments may underestimate the longer-term contribution of disturbed forests to biomass accumulation and carbon recovery. In addition, the different growth-rate distributions among forest types and disturbance classes suggest that post-disturbance dynamics in this forest should not be interpreted solely through a single mean response.

Methodologically, this study provides a practical workflow for linking field plots, harmonized multitemporal LiDAR, and high-resolution image classification for disturbance assessment, restoration planning, and biomass accounting. The framework should be transferable to other disturbance-affected forests where repeated LiDAR and inventory data are available. Remaining uncertainty is mainly associated with the CHM–AGB model, localized negative growth patches, and incomplete management-history information. Future work should incorporate independent validation datasets, stronger uncertainty diagnostics, and management records so that long-term recovery processes can be attributed more confidently and updated as new LiDAR observations become available.

This research was published as

Ang Li, Tomomichi Kato, Hantao Li, Long Duc Nguyen, Masato Hayashi, Ram Avtar, and Tatsuro Nakaji. Characterizing typhoon-disturbed biomass dynamics using multi-temporal LiDAR, high-resolution imagery, and deep learning in cool-temperate forest, northern Japan. *Forest Ecology and Management*, 610, 123692, 2026. doi:10.1016/j.foreco.2026.123692.

Acknowledgments

I would like to express my sincere gratitude to Prof. Tomomichi Kato for his overall supervision and support throughout my PhD. His guidance was important to the completion of this thesis. Visiting the experimental forest with him helped deepen my understanding of the study site and the context of this research. I also thank my co-advisors, Prof. Takashi Hirano and Prof. Shoichiro Hamamoto, for their valuable comments.

I am grateful to Dr. Masato Hayashi for his helpful suggestions and support. His comments were valuable in refining this research as the study developed. I am also grateful to Prof. Tatsuro Nakaji for his technical guidance and data support related to this research. His assistance with practical and data-related aspects of the work was important for carrying this study forward.

I also thank Hantao Li and Long Duc Nguyen for their helpful advice and support. I am grateful to Ram Avtar and Hiroyuki Oguma for their data support related to this research. In addition, I would like to thank the members of our laboratory for providing a supportive research environment. The collegial atmosphere and routine academic exchange in the lab helped maintain a stable setting for my doctoral study.

My PhD study was supported by the MEXT scholarship. I sincerely appreciate this financial support during my doctoral study at Hokkaido University.

References

Andersen, H.E., Reutebuch, S.E., McGaughey, R.J., d'Oliveira, M.V.N., Keller, M., 2014. Monitoring selective logging in western amazonia with repeat lidar flights. Remote Sensing of Environment 151, 157–165. doi:10.1016/j.rse.2013.08.049. special Issue on 2012 ForestSAT.

Anderson-Teixeira, K.J., Miller, A.D., Mohan, J.E., Hudiburg, T.W., Duval, B.D., DeLucia, E.H., 2013. Altered dynamics of forest recovery under a changing climate. Global Change Biology 19, 2001–2021. doi:10.1111/gcb.12194.

Asner, G.P., Knapp, D.E., Broadbent, E.N., Oliveira, P.J.C., Keller, M., Silva, J.N., 2005. Selective Logging in the Brazilian Amazon. Science 310, 480–482. doi:10.1126/science.1118051.

Badouard, V., Verley, P., Bai, Y., Sellan, G., Françoise, L., Marcon, E., Derroire, G., Vincent, G., 2025. Using high penetration airborne LiDAR and dense UAV scanning to produce accurate 3d maps of light availability in dense tropical forest. Agricultural and Forest Meteorology 373, 110713. doi:10.1016/j.agrformet.2025.110713.

Bartels, S.F., Chen, H.Y.H., Wulder, M.A., White, J.C., 2016. Trends in post-disturbance recovery rates of Canada's forests following wildfire and harvest. Forest Ecology and Management 361, 194–207. doi:10.1016/j.foreco.2015.11.015.

Borlaf-Mena, I., García-Duro, J., Santoro, M., Villard, L., Badea, O., Tanase, M.A., 2023. Seasonality and directionality effects on radar backscatter are key to identify mountain

forest types with sentinel-1 data. Remote Sensing of Environment 296, 113728. doi:10.1016/j.rse.2023.113728.

Brede, B., Terryn, L., Barbier, N., Bartholomeus, H.M., Bartolo, R., Calders, K., Derroire, G., Krishna Moorthy, S.M., Lau, A., Levick, S.R., Raumonen, P., Verbeeck, H., Wang, D., Whiteside, T., van der Zee, J., Herold, M., 2022. Non-destructive estimation of individual tree biomass: Allometric models, terrestrial and uav laser scanning. Remote Sensing of Environment 280, 113180. doi:10.1016/j.rse.2022.113180.

Cannon, J.B., Peterson, C.J., Godfrey, C.M., Whelan, A.W., 2023. Hurricane wind regimes for forests of North America. Proceedings of the National Academy of Sciences 120, e2309076120. doi:10.1073/pnas.2309076120.

Coops, N.C., Tompalski, P., Goodbody, T.R.H., Queinnec, M., Luther, J.E., Bolton, D.K., White, J.C., Wulder, M.A., van Lier, O.R., Hermosilla, T., 2021. Modelling lidar-derived estimates of forest attributes over space and time: A review of approaches and future trends. Remote Sensing of Environment 260, 112477. doi:10.1016/j.rse.2021.112477.

De Marzo, T., Pratzer, M., Baumann, M., Gasparri, N.I., Pötzschner, F., Kuemmerle, T., 2023. Linking disturbance history to current forest structure to assess the impact of disturbances in tropical dry forests. Forest Ecology and Management 539, 120989. doi:10.1016/j.foreco.2023.120989.

Decuyper, M., Chávez, R.O., Lohbeck, M., Lastra, J.A., Tsendbazar, N., Hackländer, J., Herold, M., Vågen, T.G., 2022. Continuous monitoring of forest change dynamics with satellite time series. Remote Sensing of Environment 269, 112829. doi:10.1016/j.rse.2021.112829.

Gan, Y., Wang, Q., Iio, A., 2023. Tree Crown Detection and Delineation in a Temperate Deciduous Forest from UAV RGB Imagery Using Deep Learning Approaches: Effects of Spatial Resolution and Species Characteristics. Remote Sensing 15, 778. doi:10.3390/rs15030778.

Garcia, M., Saatchi, S., Ferraz, A., Silva, C.A., Ustin, S., Koltunov, A., Balzter, H., 2017. Impact of data model and point density on aboveground forest biomass estimation from airborne LiDAR. Carbon Balance and Management 12, 4. doi:10.1186/s13021-017-0073-1.

Geng, Y., Yue, Q., Zhang, C., Zhao, X., von Gadow, K., 2021. Dynamics and drivers of aboveground biomass accumulation during recovery from selective harvesting in an uneven-aged forest. European Journal of Forest Research 140, 1163–1178. doi:10.1007/s10342-021-01394-9.

Hayashi, M., Saigusa, N., Oguma, H., Yamagata, Y., Takao, G., 2015. Quantitative assessment of the impact of typhoon disturbance on a Japanese forest using satellite laser altimetry. Remote Sensing of Environment 156, 216–225. doi:10.1016/j.rse.2014.09.028.

He, K., Zhang, X., Ren, S., Sun, J., 2016. Deep residual learning for image recognition, in: Proceedings of the IEEE Conference on Computer Vision and Pattern Recognition (CVPR), pp. 770–778. doi:10.1109/CVPR.2016.90.

Hethcoat, M.G., Edwards, D.P., Carreiras, J.M.B., Bryant, R.G., França, F.M., Quegan, S., 2019. A machine learning approach to map tropical selective logging. Remote Sensing of Environment 221, 569–582. doi:10.1016/j.rse.2018.11.044.

Hirata, R., Takagi, K., Ito, A., Hirano, T., Saigusa, N., 2014. The impact of climate variation

and disturbances on the carbon balance of forests in Hokkaido, Japan. Biogeosciences 11, 5139–5154. doi:10.5194/bg-11-5139-2014.

Hiura, T., 2005. Estimation of aboveground biomass and net biomass increment in a cool temperate forest on a landscape scale. Ecological Research 20, 271–277. doi:10.1007/s11284-005-0042-0.

Hojo, A., Avtar, R., Nakaji, T., Tadono, T., Takagi, K., 2023. Modeling forest above-ground biomass using freely available satellite and multisource datasets. Ecological Informatics 74, 101973. doi:10.1016/j.ecoinf.2023.101973.

Hudak, A.T., Strand, E.K., Vierling, L.A., Byrne, J.C., Eitel, J.U.H., Martinuzzi, S., Falkowski, M.J., 2012. Quantifying aboveground forest carbon pools and fluxes from repeat LiDAR surveys. Remote Sensing of Environment 123, 25–40. doi:10.1016/j.rse.2012.02.023.

Ishihara, M.I., Utsugi, H., Tanouchi, H., Aiba, M., Kurokawa, H., Onoda, Y., Nagano, M., Umehara, T., Ando, M., Miyata, R., Hiura, T., 2015. Efficacy of generic allometric equations for estimating biomass: A test in Japanese natural forests. Ecological Applications 25, 1433–1446. doi:10.1890/14-0175.1.

Jucker, T., Caspersen, J., Chave, J., Antin, C., Barbier, N., Bongers, F., Dalponte, M., van Ewijk, K.Y., Forrester, D.I., Haeni, M., Higgins, S.I., Holdaway, R.J., Iida, Y., Lorimer, C., Marshall, P.L., Momo, S., Moncrieff, G.R., Ploton, P., Poorter, L., Rahman, K.A., Schlund, M., Sonké, B., Sterck, F.J., Trugman, A.T., Usoltsev, V.A., Vanderwel, M.C., Waldner, P., Wedeux, B.M.M., Wirth, C., Wöll, H., Woods, M., Xiang, W., Zimmermann, N.E., Coomes, D.A., 2017. Allometric equations for integrating remote sensing imagery

into forest monitoring programmes. Global Change Biology 23, 177–190. doi:10.1111/gcb.13388.

Khosravipour, A., Skidmore, A.K., Isenburg, M., 2016. Generating spike-free digital surface models using LiDAR raw point clouds: A new approach for forestry applications. International Journal of Applied Earth Observation and Geoinformation 52, 104–114. doi:10.1016/j.jag.2016.06.005.

Khosravipour, A., Skidmore, A.K., Isenburg, M., Wang, T., Hussin, Y.A., 2014. Generating Pit-free Canopy Height Models from Airborne Lidar. Photogrammetric Engineering & Remote Sensing 80, 863–872. doi:10.14358/PERS.80.9.863.

Knapp, N., Fischer, R., Cazcarra-Bes, V., Huth, A., 2020. Structure metrics to generalize biomass estimation from lidar across forest types from different continents. Remote Sensing of Environment 237, 111597. doi:10.1016/j.rse.2019.111597.

Lian, X., Morfopoulos, C., Gentine, P., 2024. Water deficit and storm disturbances coregulate Amazon rainforest seasonality. Science Advances 10, eadk5861. doi:10.1126/sciadv.adk5861.

Loh, H.Y., James, D., Ioki, K., Wong, W.V.C., Tsuyuki, S., Phua, M.H., 2022. Estimating aboveground biomass changes in a human-modified tropical montane forest of borneo using multi-temporal airborne lidar data. Remote Sensing Applications: Society and Environment 28, 100821. doi:10.1016/j.rsase.2022.100821.

Mack, M.C., Walker, X.J., Johnstone, J.F., Alexander, H.D., Melvin, A.M., Jean, M., Miller, S.N., 2021. Carbon loss from boreal forest wildfires offset by increased dominance of deciduous trees. Science 372, 280–283. doi:10.1126/science.abf3903.

Mandl, L., Viana-Soto, A., Seidl, R., Stritih, A., Senf, C., 2024. Unmixing-based forest recovery indicators for predicting long-term recovery success. Remote Sensing of Environment 308, 114194. doi:10.1016/j.rse.2024.114194.

Matasci, G., Hermosilla, T., Wulder, M.A., White, J.C., Coops, N.C., Hobart, G.W., Bolton, D.K., Tompalski, P., Bater, C.W., 2018. Three decades of forest structural dynamics over Canada's forested ecosystems using Landsat time-series and LiDAR plots. Remote Sensing of Environment 216, 697–714. doi:10.1016/j.rse.2018.07.024.

Mayra, J., Keski-Saari, S., Kivinen, S., Tanhuanpaa, T., Hurskainen, P., Kullberg, P., Poikolainen, L., Viinikka, A., Tuominen, S., Kumpula, T., Vihervaara, P., 2021. Tree species classification from airborne hyperspectral and LiDAR data using 3D convolutional neural networks. Remote Sensing of Environment 256, 112322. doi:10.1016/j.rse.2021.112322.

Negrón-Juárez, R.I., Chambers, J.Q., Guimaraes, G., Zeng, H., Raupp, C.F.M., Marra, D.M., Ribeiro, G.H.P.M., Saatchi, S.S., Nelson, B.W., Higuchi, N., 2010. Widespread Amazon forest tree mortality from a single cross-basin squall line event. Geophysical Research Letters 37, L16701. doi:10.1029/2010GL043733.

Ogawa, H., 1969. An attempt at classifying forest types based on the relationship between tree height and breast height diameter (DBH), in: Kira, T. (Ed.), Comparative study of primary productivity in forest ecosystems. JIBP-PT-F progress report for 1968, pp. 3–17.

Pan, Y., Birdsey, R.A., Fang, J., Houghton, R., Kauppi, P.E., Kurz, W.A., Phillips, O.L., Shvidenko, A., Lewis, S.L., Canadell, J.G., Ciais, P., Jackson, R.B., Pacala, S.W., McGuire, A.D., Piao, S., Rautiainen, A., Sitch, S., Hayes, D., 2011. A Large and Per-

sistent Carbon Sink in the World's Forests. Science 333, 988–993. doi:10.1126/science.1201609.

Pascual, A., 2019. Using tree detection based on airborne laser scanning to improve forest inventory considering edge effects and the co-registration factor. Remote Sensing 11, 2675. doi:10.3390/rs11222675.

Pimont, F., Allard, D., Soma, M., Dupuy, J.L., 2018. Estimators and confidence intervals for plant area density at voxel scale with T-LiDAR. Remote Sensing of Environment 215, 343–370. doi:10.1016/j.rse.2018.06.024.

Poorter, L., Bongers, F., Aide, T.M., Almeyda Zambrano, A.M., Balvanera, P., Becknell, J.M., Boukili, V., Brancalion, P.H.S., Broadbent, E.N., Chazdon, R.L., Craven, D., de Almeida-Cortez, J.S., Cabral, G.A.L., de Jong, B.H.J., Denslow, J.S., Dent, D.H., DeWalt, S.J., Dupuy, J.M., Durán, S.M., Espírito-Santo, M.M., Fandino, M.C., César, R.G., Hall, J.S., Hernandez-Stefanoni, J.L., Jakovac, C.C., Junqueira, A.B., Kennard, D., Letcher, S.G., Licona, J.C., Lohbeck, M., Marín-Spiotta, E., Martínez-Ramos, M., Massoca, P., Meave, J.A., Mesquita, R., Mora, F., Muñoz, R., Muscarella, R., Nunes, Y.R.F., Ochoa-Gaona, S., de Oliveira, A.A., Orihuela-Belmonte, E., Peña-Claros, M., Pérez-García, E.A., Piotto, D., Powers, J.S., Rodríguez-Velázquez, J., Romero-Pérez, I.E., Ruíz, J., Saldarriaga, J.G., Sanchez-Azofeifa, A., Schwartz, N.B., Steininger, M.K., Swenson, N.G., Toledo, M., Uriarte, M., van Breugel, M., van der Wal, H., Veloso, M.D.M., Vester, H.F.M., Vicentini, A., Vieira, I.C.G., Bentos, T.V., Williamson, G.B., Rozendaal, D.M.A., 2016. Biomass resilience of Neotropical secondary forests. Nature 530, 211–214. doi:10.1038/nature16512.

Pugh, T.A.M., Lindeskog, M., Smith, B., Poulter, B., Arneth, A., Haverd, V., Calle, L.,

2019. Role of forest regrowth in global carbon sink dynamics. Proceedings of the National Academy of Sciences 116, 4382–4387. doi:10.1073/pnas.1810512116.

Requena Suarez, D., Rozendaal, D.M.A., De Sy, V., Decuyper, M., Málaga, N., Durán Montesinos, P., Arana Olivos, A., De la Cruz Paiva, R., Martius, C., Herold, M., 2023. Forest disturbance and recovery in Peruvian Amazonia. Global Change Biology 29, 3601–3621. doi:10.1111/gcb.16695.

Requena Suarez, D., Rozendaal, D.M.A., De Sy, V., Phillips, O.L., Alvarez-Dávila, E., Anderson-Teixeira, K., Araujo-Murakami, A., Arroyo, L., Baker, T.R., Bongers, F., Brienen, R.J.W., Carter, S., Cook-Patton, S.C., Feldpausch, T.R., Griscom, B.W., Harris, N., Hérault, B., Honorio Coronado, E.N., Leavitt, S.M., Lewis, S.L., Marimon, B.S., Monteagudo Mendoza, A., Kassi N'dja, J., N'Guessan, A.E., Poorter, L., Qie, L., Rutishauser, E., Sist, P., Sonké, B., Sullivan, M.J.P., Vilanova, E., Wang, M.M.H., Martius, C., Herold, M., 2019. Estimating aboveground net biomass change for tropical and subtropical forests: Refinement of IPCC default rates using forest plot data. Global Change Biology 25, 3609–3624. doi:10.1111/gcb.14767.

Riofrío, J., White, J.C., Tompalski, P., Coops, N.C., Wulder, M.A., 2023. Modelling height growth of temperate mixedwood forests using an age-independent approach and multi-temporal airborne laser scanning data. Forest Ecology and Management 543, 121137. doi:10.1016/j.foreco.2023.121137.

Roussel, J.R., Caspersen, J., Béland, M., Thomas, S., Achim, A., 2017. Removing bias from LiDAR-based estimates of canopy height: Accounting for the effects of pulse density and footprint size. Remote Sensing of Environment 198, 1–16. doi:10.1016/j.rse.2017.05.032.

Sano, T., Hirano, T., Liang, N., Hirata, R., Fujinuma, Y., 2010. Carbon dioxide exchange of a larch forest after a typhoon disturbance. Forest Ecology and Management 260, 2214–2223. doi:10.1016/j.foreco.2010.09.026.

Takahashi, A., Oguma, H., Shimada, M., Watanabe, M., Yone, Y., Saigusa, N., 2011. Influence of forest disturbances on backscatter of the airborne L-band synthetic-aperture radar in a larch forest in northern Japan. Hydrological Research Letters 5, 64–68. doi:10.3178/hrl.5.64.

Takano, K.T., Nakagawa, K., Aiba, M., Oguro, M., Morimoto, J., Furukawa, Y., Mishima, Y., Ogawa, K., Ito, R., Takemi, T., 2016. Projection of impacts of climate change on windthrows and evaluation of potential adaptation measures in forest management: A case study from empirical modelling of windthrows in Hokkaido, Japan, by Typhoon Songda (2004). Hydrological Research Letters 10, 132–138. doi:10.3178/hrl.10.132.

Walker, A.P., De Kauwe, M.G., Medlyn, B.E., Zaehle, S., Iversen, C.M., Asao, S., Guenet, B., Harper, A., Hickler, T., Hungate, B.A., Jain, A.K., Luo, Y., Lu, X., Lu, M., Luus, K., Megonigal, J.P., Oren, R., Ryan, E., Shu, S., Talhelm, A., Wang, Y.P., Warren, J.M., Werner, C., Xia, J., Yang, B., Zak, D.R., Norby, R.J., 2019. Decadal biomass increment in early secondary succession woody ecosystems is increased by CO2 enrichment. Nature Communications 10, 454. doi:10.1038/s41467-019-08348-1.

Wang, J.A., Baccini, A., Farina, M., Randerson, J.T., Friedl, M.A., 2021. Disturbance suppresses the aboveground carbon sink in north american boreal forests. Nature Climate Change 11, 435–441. doi:10.1038/s41558-021-01027-4.

Wolf, S., Paul-Limoges, E., 2023. Drought and heat reduce forest carbon uptake. Nature Communications 14, 6217. doi:10.1038/s41467-023-41854-x.

Wu, L., Kato, T., Sato, H., Hirano, T., Yazaki, T., 2019. Sensitivity analysis of the typhoon disturbance effect on forest dynamics and carbon balance in the future in a cool-temperate forest in northern Japan by using SEIB-DGVM. Forest Ecology and Management 451, 117529. doi:10.1016/j.foreco.2019.117529.

Yazaki, T., Hirano, T., Sano, T., 2016. Biomass accumulation and net primary production during the early stage of secondary succession after a severe forest disturbance in northern japan. Forests 7, 287. doi:10.3390/f7110287.

Yun, T., Jiang, K., Li, G., Eichhorn, M.P., Fan, J., Liu, F., Chen, B., An, F., Cao, L., 2021. Individual tree crown segmentation from airborne LiDAR data using a novel Gaussian filter and energy function minimization-based approach. Remote Sensing of Environment 256, 112307. doi:10.1016/j.rse.2021.112307.